Supporting Information

Electrochemical amorphous-to-1T-phase reconfiguration of Ru-W bimetallic sulfide for sustainable hydrogen evolution

Jingchun Wang[a‡], Xiao Yu[b‡], Yan Sun[a*], Yipeng Zang[c], Xujiang Yu[d], Haolan Tao[b*], Cheng Lian[b*], Huibin Qiu[a*]

Table of Contents

1. Supplementary methods

Chemicals

Ruthenium chloride hydrate ($RuCl_3 \cdot xH_2O$, 98%), ammonium tetrathiotungstate (VI) ($(NH4)_2WS_4$, 99.9%), isopropanol (99.8%, HPLC), and tetrahydrofuran (99.8%, HPLC) were all purchased from Aladdin. Ethanol (≥ 99.5%, GR) was sourced from Reagent. Unless otherwise stated, all chemicals were directly utilized in their as-received state without additional purification steps. Carbon cloth was purchased from SINERO. Before use, the received carbon cloth was ultrasonically treated in acetone, then alternately rinsed with water and ethanol to remove surface-adsorbed components, and finally dried naturally.

Synthesis of polymer

PS_{480}-*b*-$P2VP_{490}$ block copolymer (the subscripts indicate the degree of polymerization of the corresponding block) was synthesized by sequential anionic polymerization reactions in a glove box under an inert atmosphere according to the previously reported method.[1]

Preparation of micellar film

In a typical process, 100 mg of PS_{480}-*b*-$P2VP_{490}$ block copolymer solid was fully dissolved in 10 mL of tetrahydrofuran (THF) to achieve a solution of PS_{480}-*b*-$P2VP_{490}$ unimers. Subsequently, 50 μL of the solution was uniformly casted on a desired substrate (e.g., carbon cloth, glass, silicon wafer, etc.) that had been pre-treated with plasma. The sample was dried at room temperature, allowing the natural evaporation of THF.

Preparation of RuWS-accumulated micellar film

Typically, the above micellar film on a substrate was firstly immersed into an ethanol solution of Ru^{3+} ions ($RuCl_3$, 0.10 mol/mL). After 3 h, the sample was rinsed with isopropanol three times to remove the excess Ru^{3+} ions, followed by immersion in a mixture of 1 : 1 (*v*/*v*) isopropanol and water containing WS_4^{2-} ions ($(NH4)_2WS_4$, 0.0287 mol/mL) for 6 h. Finally, the resulting sample was allowed to dry under a gentle stream of nitrogen.

Preparation of amorphous mesoporous RuWS film

Typically, RuWS-accumulated micellar film was pyrolyzed at a certain temperature (300, 400, 500 and 600 °C) in nitrogen for 5 h to yield amorphous mesoporous RuWS film.

Preparation of non-mesostructured RuWS powder

Typically, 50 mg of $RuCl_3$ and 145 mg of $(NH4)_2WS_4$ were dissolved in 100 mL of a mixture of 1 : 1 (*v*/*v*) ethanol and water. After 24 h of aging, co-precipitation occurred. The precipitate was collected by centrifugation and subsequently dried under vacuum for 12 h to obtain the RuWS powder.

Materials characterization

Scanning electron microscopy (SEM) was performed on a TESCAN MAIA3 microscope operating at an accelerating voltage of 5 kV under high vacuum conditions. All specimens were pre-coated with a thin platinum (Pt) layer to enhance the conductivity and image quality. Transmission electron microscopy (TEM) was performed using a Thermo Scientific Talos L120C G2 microscope operating at an acceleration voltage of 120 kV. High-resolution TEM (HRTEM), high-angle annular dark-field scanning transmission electron microscopy (HAADF-STEM), and spatially resolved energy-dispersive X-ray spectroscopy (EDS) elemental mapping, were conducted on a Thermo Scientific Talos F200X microscope, working at 200 kV for optimal analytical performance. Crystallographic analysis was performed using X-ray diffraction (XRD) on a Japan Rigaku Mini Flex 600 diffractometer equipped with Cu Kα radiation (40 kV, 40 mA). Surface chemical composition was investigated via X-ray photoelectron spectroscopy (XPS) conducted on a Kratos AXIS UltraDLD instrument utilizing Al Kα radiation (1486 eV). Nitrogen sorption measurements were conducted on a Micromeritics ASAP 2050 instrument. X-ray absorption fine structure (XAFS) spectra were collected at the BL13SSW beamline of Shanghai Synchrotron Radiation Facility (SSRF), operating at an electron energy of 2.5 GeV with a maximum beam current of 250 mA in total fluorescence-yield mode. The acquired extended XAFS (EXAFS) data were subjected to Fourier transform analysis and processed following standard protocols using the ATHENA module within the IFEFFIT software package for quantitative structural determination. Fourier transform infrared spectroscopy (FT-IR) was carried out using a PERKINELMER Spectrum 100 Spectroscopy. Raman microscopy was accomplished on a Horiba LabRAM Solei spectrometer. Ultraviolet-Visible (UV-vis) absorption spectra was collected using PERKINELMER Lambda 750S. Elemental composition was analyzed using inductively coupled plasma-optical emission spectrometer (ICP-OES) on a Thermo Fisher iCAP PRO system. Surface wettability characterization was carried out through contact angle measurements at room temperature using a Lauda Scientific LSA100 system equipped with a high-speed camera.

Electrochemical measurements

All the electrochemical measurements were conducted on a CHI Instrument (Chenhua CHI760E) electrochemical workstation in a three-electrode system at room temperature in 1.0 M KOH. The as-prepared samples on carbon cloth, an Ag/AgCl (3.0 M KCl) electrode and graphite rod were used as the working, reference and counter electrodes, respectively. The Ru content of a-RuWS determined by the ICP-OES was 10.51 wt%, the mass loading of Ru on the electrode was ~0.060 mg cm^{-2}. Regarding the powder catalysts, 2.0 mg of powder and 20 μL of Nafion solution were dispersed in 0.8 mL of a mixture of 1 : 1 (*v*/*v*) water and ethanol and sonicated for 20 min to obtain a homogeneous ink with a concentration of 2 mg mL^{-1}. The working electrode was fabricated by dropping 250 μL of catalyst ink onto a carbon cloth (~1.0 cm^2) and dried at 60 ºC. The mass loading of Pt/C, c-Ru/WS_2 and c-WS_2 on the electrode are 0.50 mg cm^{-2}. Linear sweep voltammetry (LSV) curves were performed at a scan rate of 5 mV s^{-1} with *iR*-correction ($\boldsymbol{E_{\mathrm{iR-corrected}} = E_{\mathrm{original}} - I \times iR_s}$). The stability of the catalysts was assessed at the potential of -0.01, -0.05, and -0.2 V vs. RHE without *iR*-correction for by chronopotentiometry measurements. No electrolyte replacement was performed during the entire stability test to maintain consistent environmental parameters. Electrochemical impedance spectroscopy (EIS) measurements were recorded at a potential of -0.01 V (*vs*. RHE) for HER with a frequency range of 0.01 Hz to 100 kHz (10 mV amplitude). The cyclic voltammogram (CV) were conducted in the double layer region (without faradaic processes) at different scan rates to determine the electrochemical double-layer capacitance (C_{dl}). All recorded related potentials were referenced to the reversible hydrogen electrode (RHE) using the following conversion equation:

$$\boldsymbol{E_{\mathrm{RHE}} = E_{\mathrm{Ag/AgCl}} + E^{0}_{\mathrm{Ag/AgCl}} + 0.059 \times \mathrm{pH}}.$$

Tafel slopes were derived by fitting the linear regions of the polarization curves at low overpotentials to the Tafel equation ($\eta = \mathbf{b} \times \log \boldsymbol{j} + \mathbf{a}$, where η is overpotential, j is the current density, and b is the Tafel slope).

Computational details

First-principles calculations were employed using the Vienna ab initio simulation package (VASP)[2-4] with the projector-augmented wave (PAW) method to investigate the phase transitions. The exchange–correlation functionals was treated by the Perdew–Burke–Ernzerhof (PBE) functional[5]. The cut-off energy for the plane-wave expansion was 500 eV. The D3 correction

method was adopted to illustrate the long-range dispersion interactions[6]. To minimize energetically the interlayer interactions between layers with periodic images, a vacuum over 20 Å was adopted. The Brillouin zone integration was performed on the ($3\times3\times1$) Gamma-centered k-point mesh for the relaxation and self-consistent step. The convergence criteria for structure optimization of these systems are the total energy change less than 10^{-5} eV and the the residual atomic forces less than 0.02 eV/Å. The analysis of electronic properties was carried using the VASPKIT program[7].

2. Supplementary figures

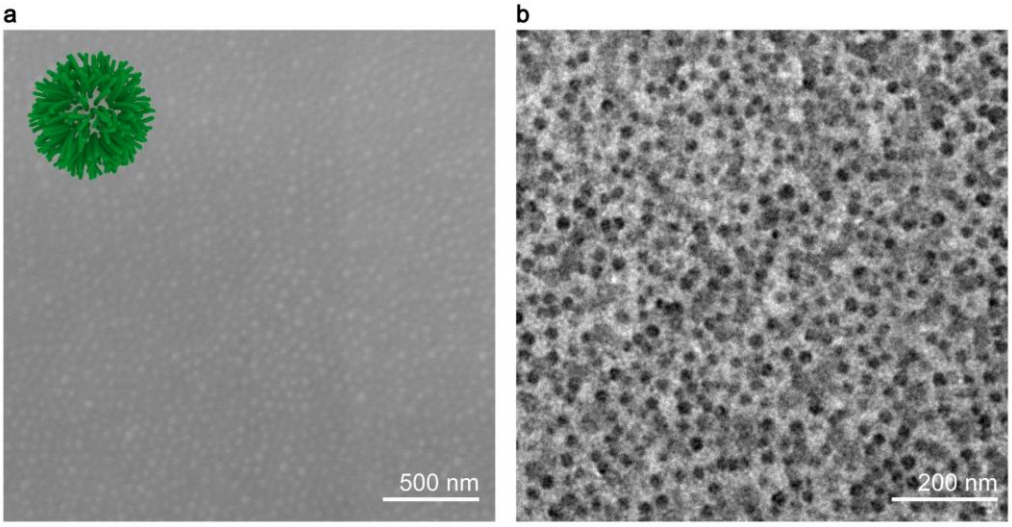

Fig. S1. Feature of PS-*b*-P2VP micellar film. (a) SEM and (b) TEM images of PS-*b*-P2VP micellar film.

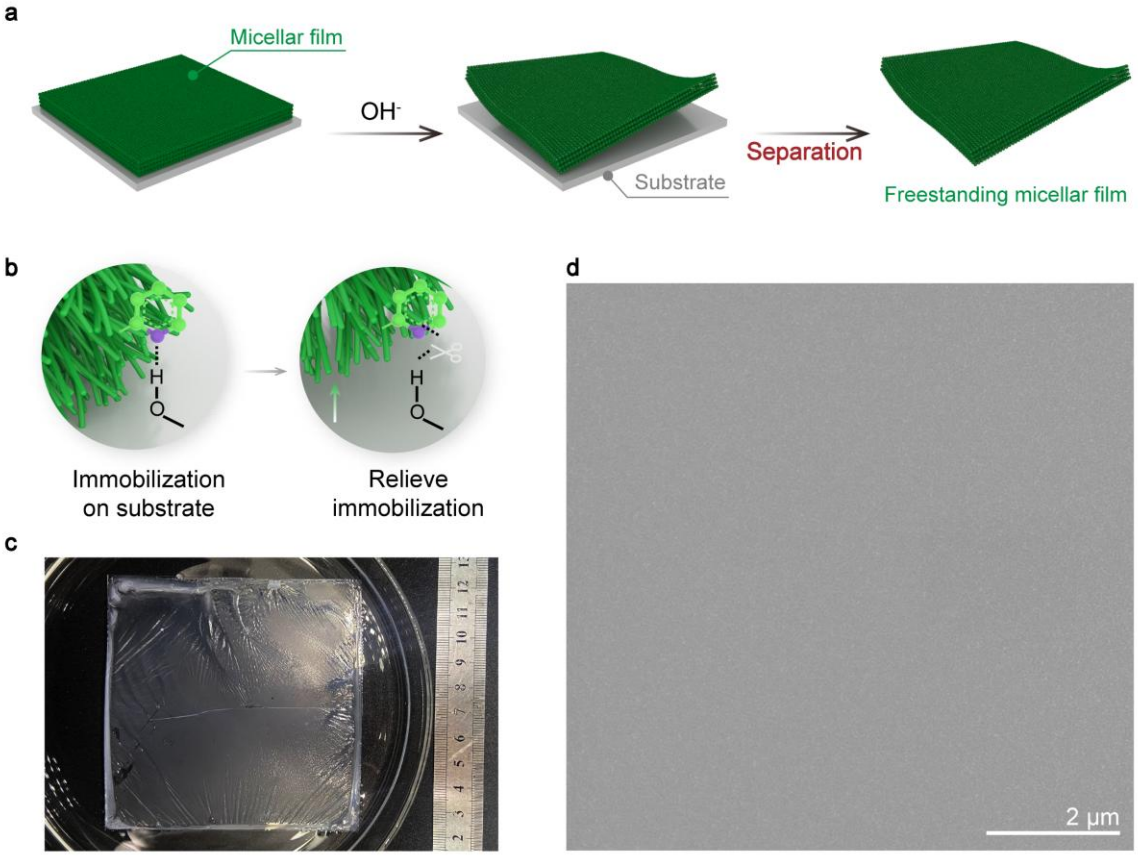

Fig. S2. Preparation of free-standing PS-*b*-P2VP micellar film. (a) Schematic illustration of the separation of micellar film from the substrate via KOH solvent treatment to form a free-standing film. (b) Schematic illustration of the separation mechanism. (c) Photograph of a piece of large-area PS-*b*-P2VP micellar film (10 cm×10 cm) peeled from the glass substrate and subsequently stored in deionized water. (d) SEM image of PS-*b*-P2VP micellar film.

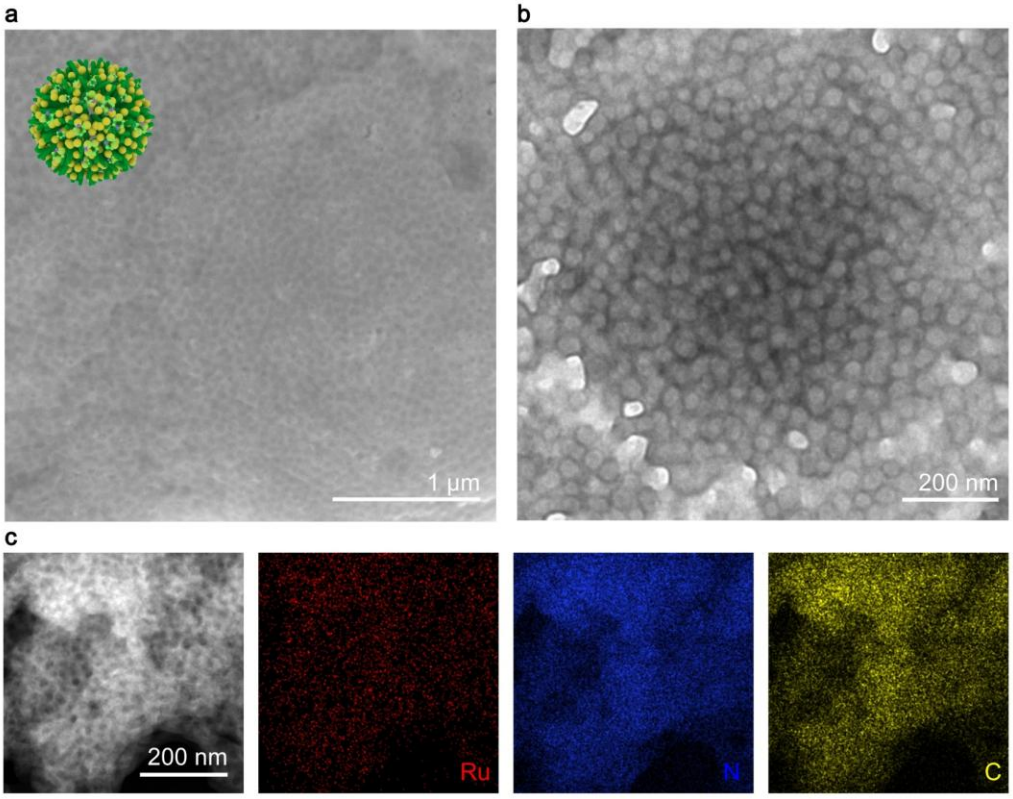

Fig. S3. Ru^{3+}-accumulated micellar film. (a) SEM, (b) TEM, and (c) HAADF-STEM and elemental mapping images of Ru^{3+}-accumulated PS-*b*-P2VP micellar film.

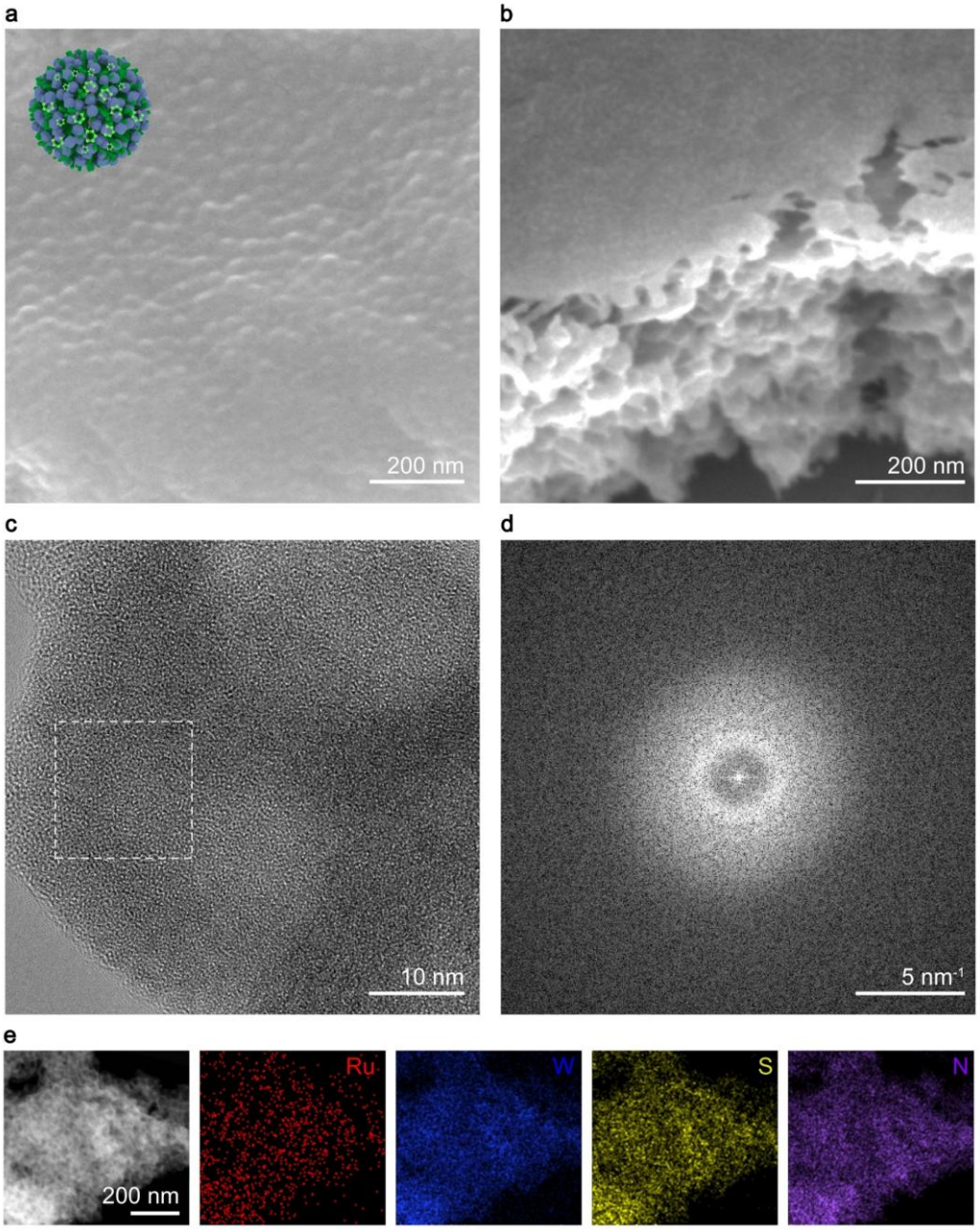

Fig. S4. RuWS-accumulated micellar film. (a, b) SEM images, (c) HRTEM image, (d) corresponding fast Fourier transform (FFT) image with characteristic weak diffusion ring, and (e) HAADF-STEM and elemental mapping images of RuWS-accumulated PS-*b*-P2VP micellar film.

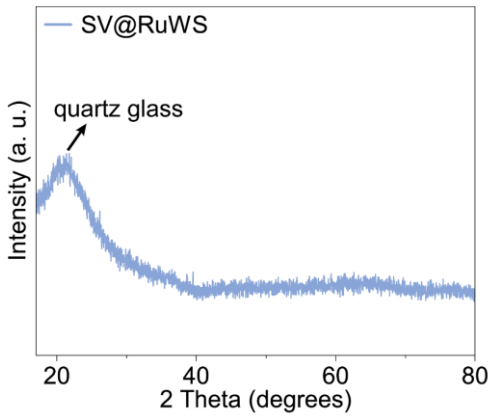

Fig. S5. XRD pattern of RuWS-accumulated PS-*b*-P2VP micellar film.

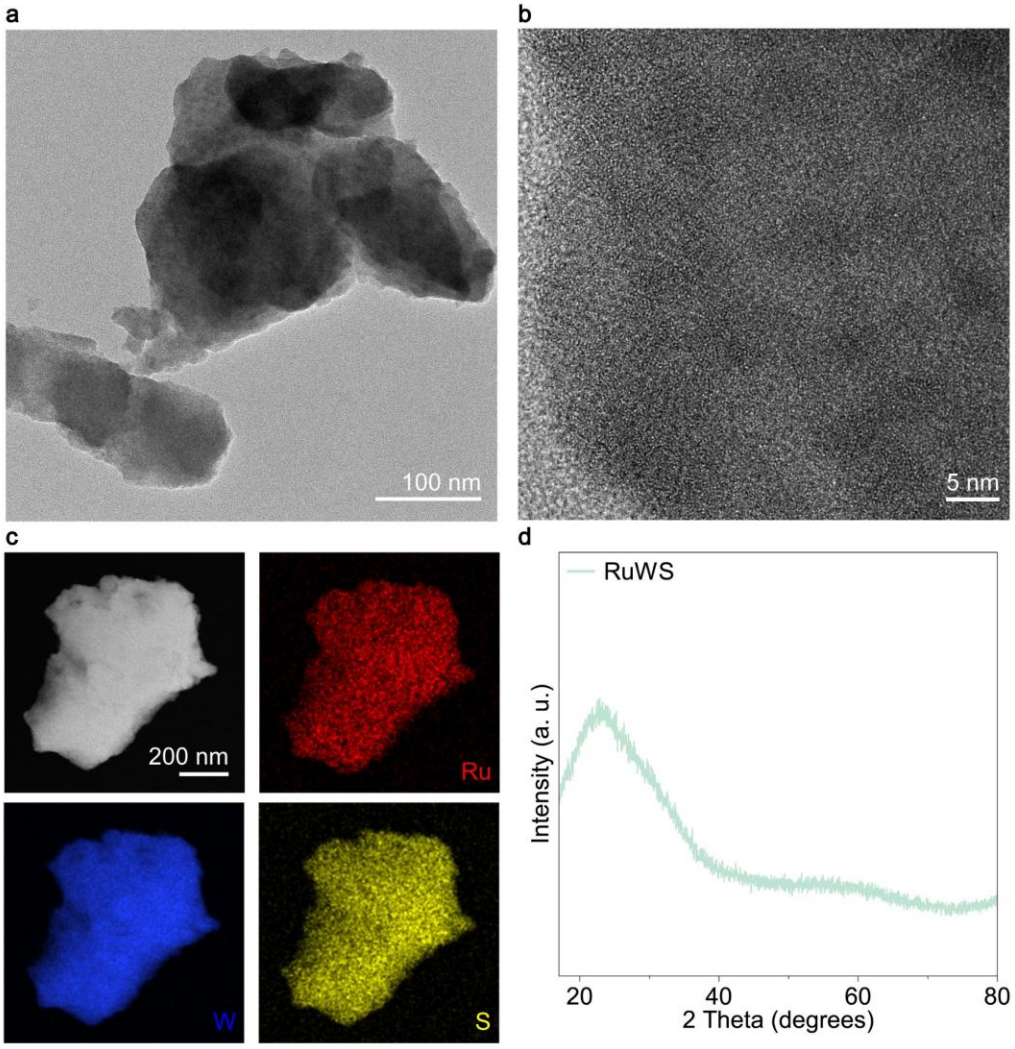

Fig. S6. RuWS powder prepared by direct co-precipitation. (a) TEM, (b) HRTEM, (c) HAADF-STEM and elemental mapping images, and (d) XRD pattern of RuWS powder.

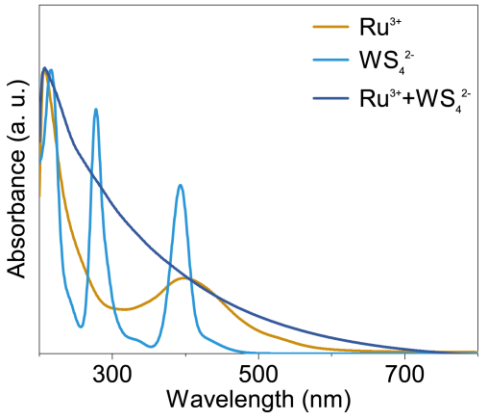

Fig. S7. Interaction between metal species. UV-vis spectra of typical solutions with Ru^{3+} ions, WS_4^{2-} ions, and both Ru^{3+} and WS_4^{2-} ions.

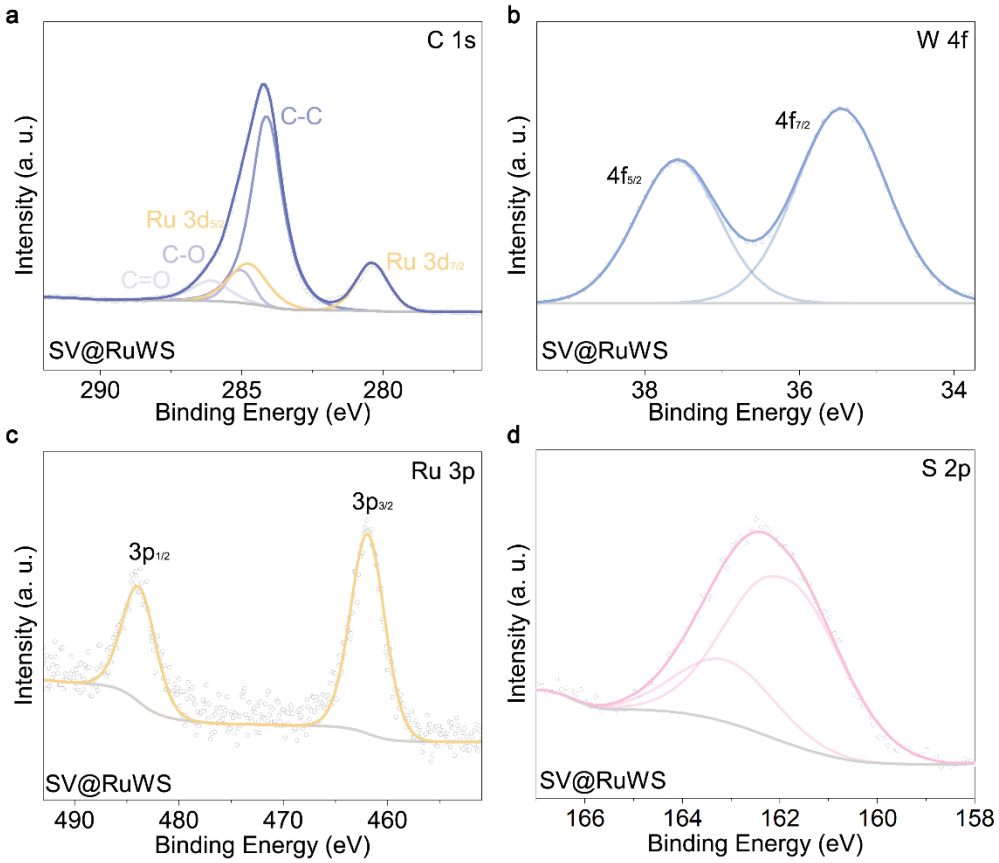

Fig. S8. High-resolution XPS spectra of (a) C 1s, (b) W 4f, (c) Ru 3p, and (d) S 2p of RuWS-accumulated PS-*b*-P2VP micellar film.

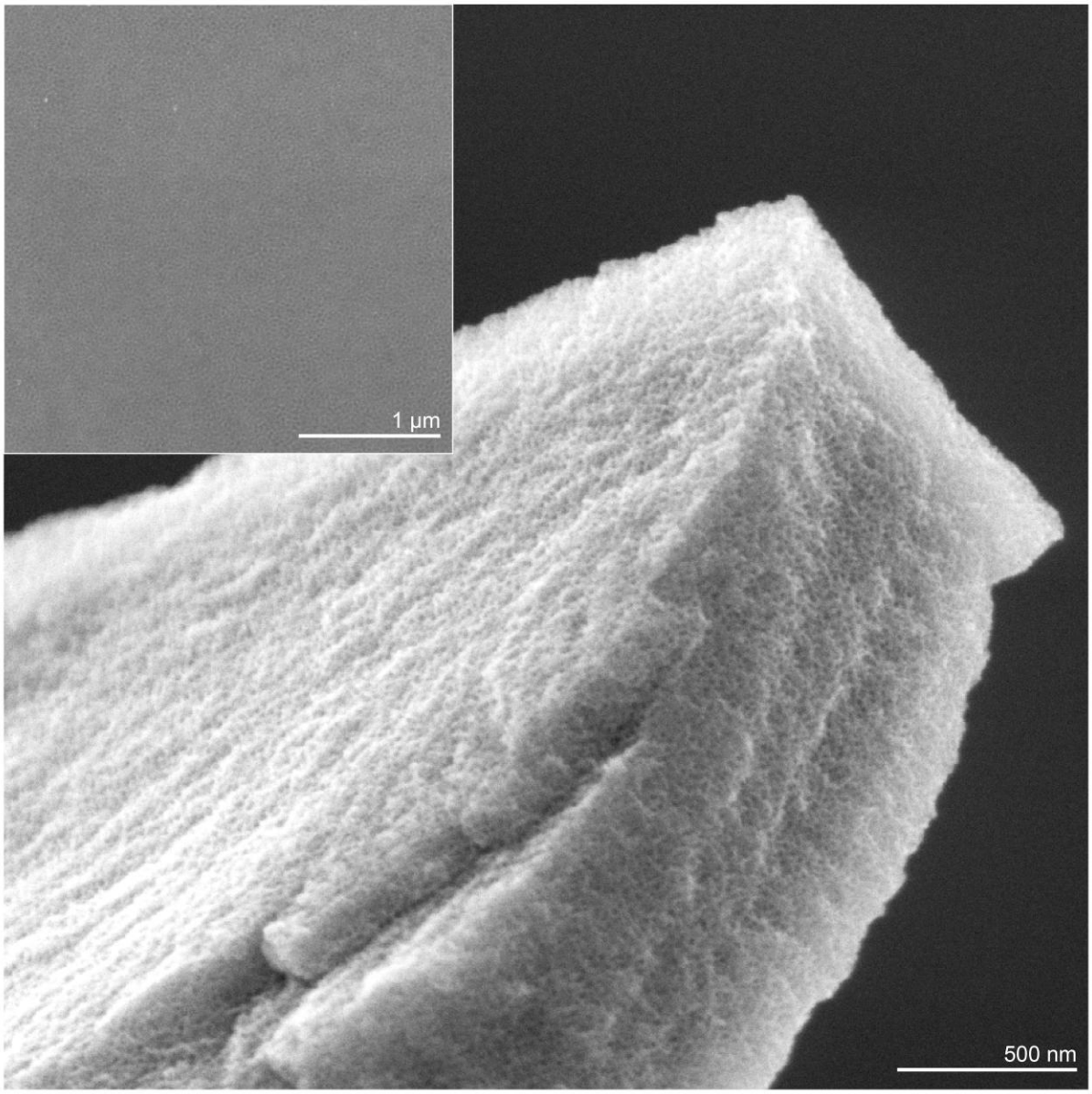

Fig. S9. Morphology of amorphous mesoporous RuWS film. SEM images of amorphous mesoporous RuWS film formed after pyrolysis of RuWS-accumulated PS-*b*-P2VP micellar film at 600 ℃ in nitrogen for 5 h. Insert is a top view SEM image of the film.

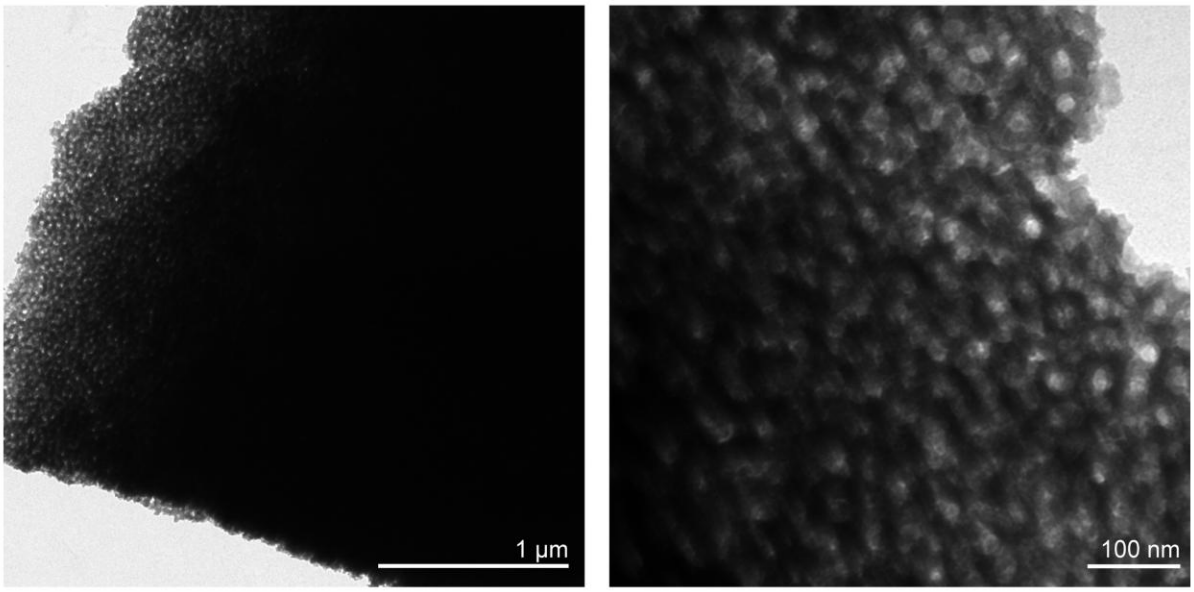

Fig. S10. Structure of amorphous mesoporous RuWS film. TEM images of amorphous mesoporous RuWS film formed after pyrolysis of RuWS-accumulated PS-*b*-P2VP micellar film at 600 ℃ in nitrogen for 5 h.

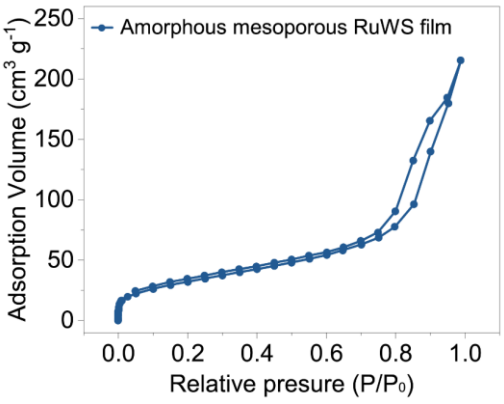

Fig. S11. Nitrogen sorption isotherm of amorphous mesoporous RuWS film formed after pyrolysis of RuWS-accumulated PS-*b*-P2VP micellar film at 600 ℃ in nitrogen for 5 h.

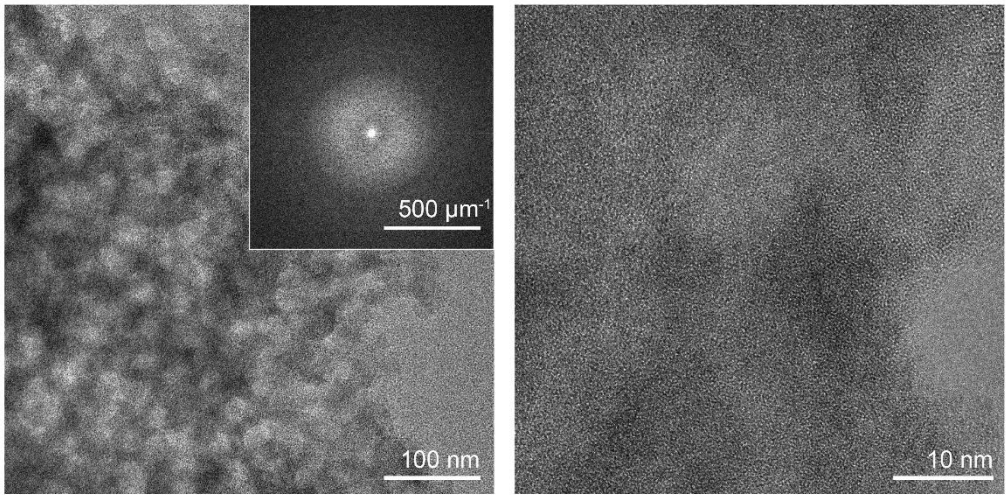

Fig. S12. HRTEM images of amorphous mesoporous RuWS film formed after pyrolysis of RuWS-accumulated PS-*b*-P2VP micellar film at 600 ℃ in nitrogen for 5 h. Insert is the corresponding FFT image with characteristic weak diffusion ring.

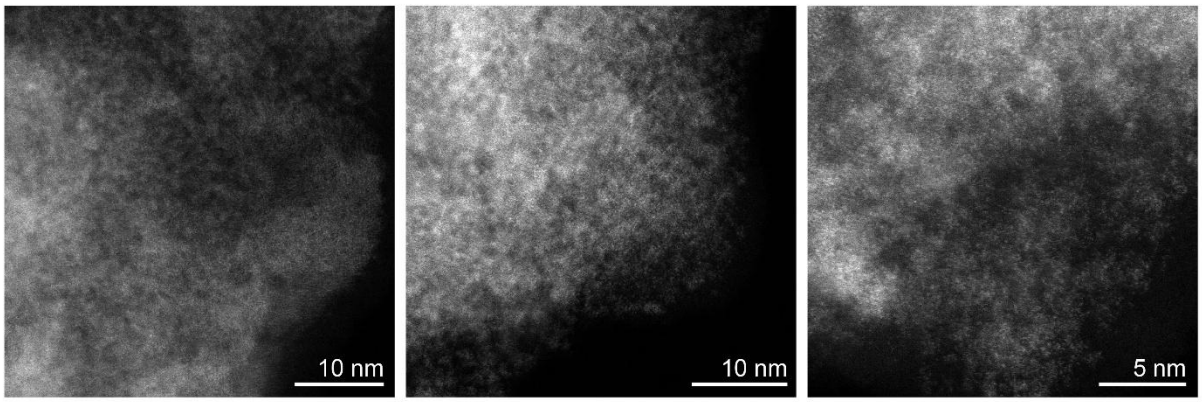

Fig. S13. AC-HAADF-STEM image of amorphous mesoporous RuWS film.

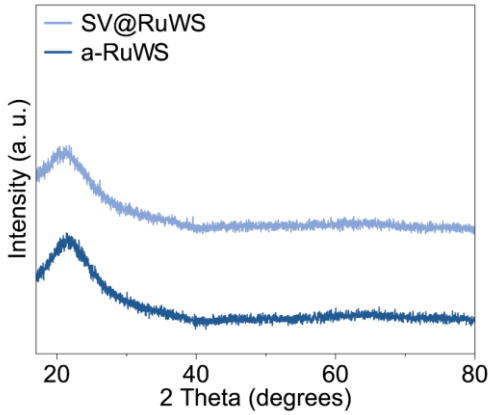

Fig. S14. XRD patterns of RuWS-accumulated PS-*b*-P2VP micellar film and amorphous mesoporous RuWS film formed after pyrolysis at 600 ℃ in nitrogen for 5 h (denoted as SV@RuWS and a-RuWS, respectively). No obvious diffraction peaks were detected, indicating a amorphous structure.

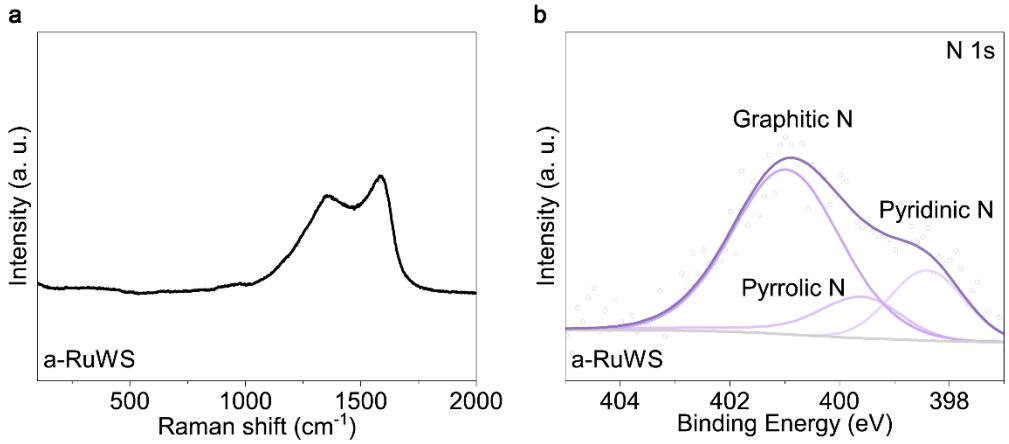

Fig. S15. (a) Raman and (b) XPS spectrum of N 1s of amorphous mesoporous RuWS film.

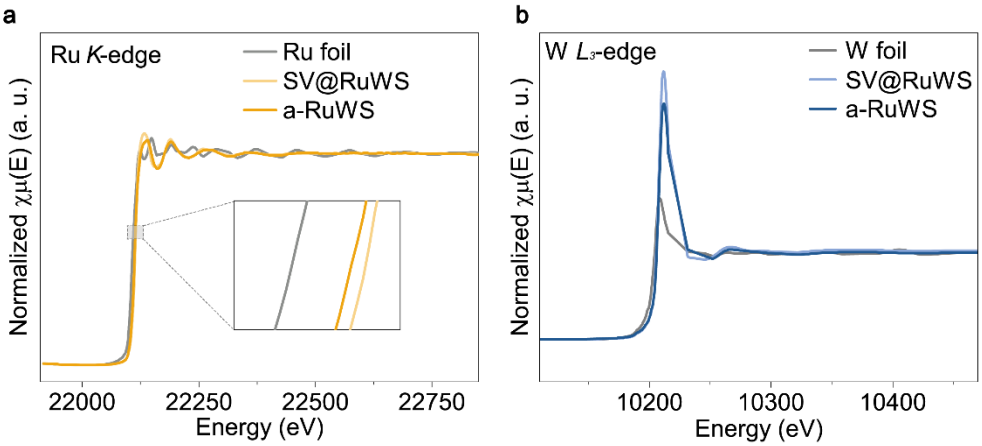

Fig. S16. XANES analysis. XANES spectra at the (a) Ru *K*-edge and (b) W L_3-edge of RuWS-accumulated micellar film and the derived amorphous mesoporous RuWS film formed after pyrolysis at 600 ℃ (denoted as SV@RuWS and a-RuWS, respectively).

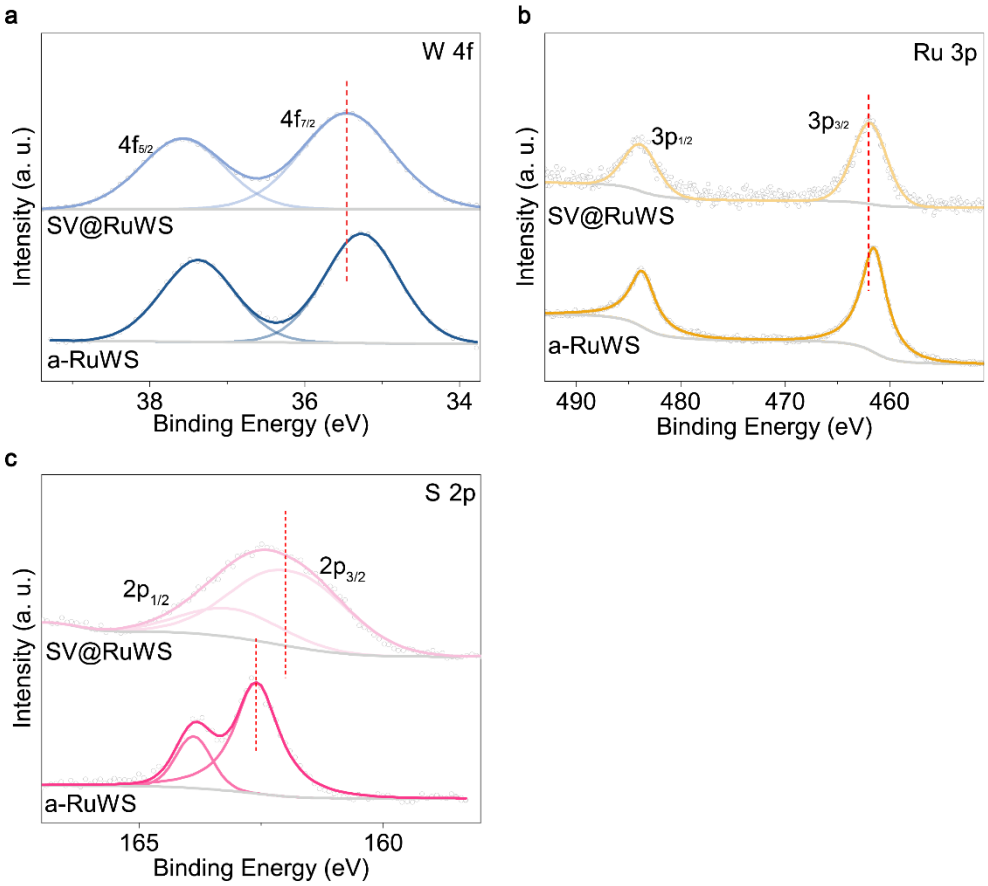

Fig. S17. XPS analysis. High-resolution XPS spectra of (a) W 4f, (b) Ru 3p, and (c) S 2p of RuWS-accumulated micellar film and the derived amorphous mesoporous RuWS film formed after pyrolysis at 600 ℃ (denoted as SV@RuWS and a-RuWS, respectively).

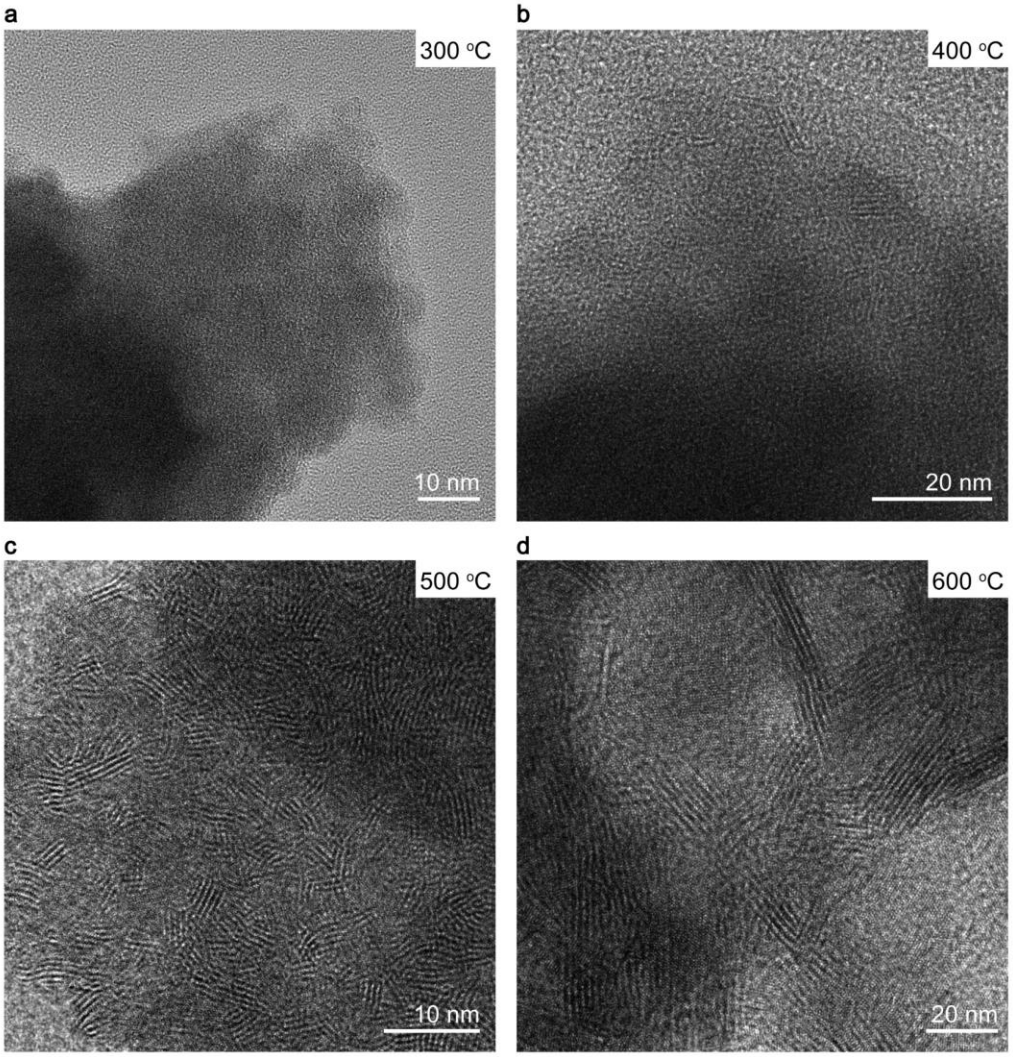

Fig. S18. RuWS powder formed after pyrolysis at different temperatures. TEM images of RuWS powder after pyrolysis at (a) 300, (b) 400, (c) 500, and (d) 600 ℃.

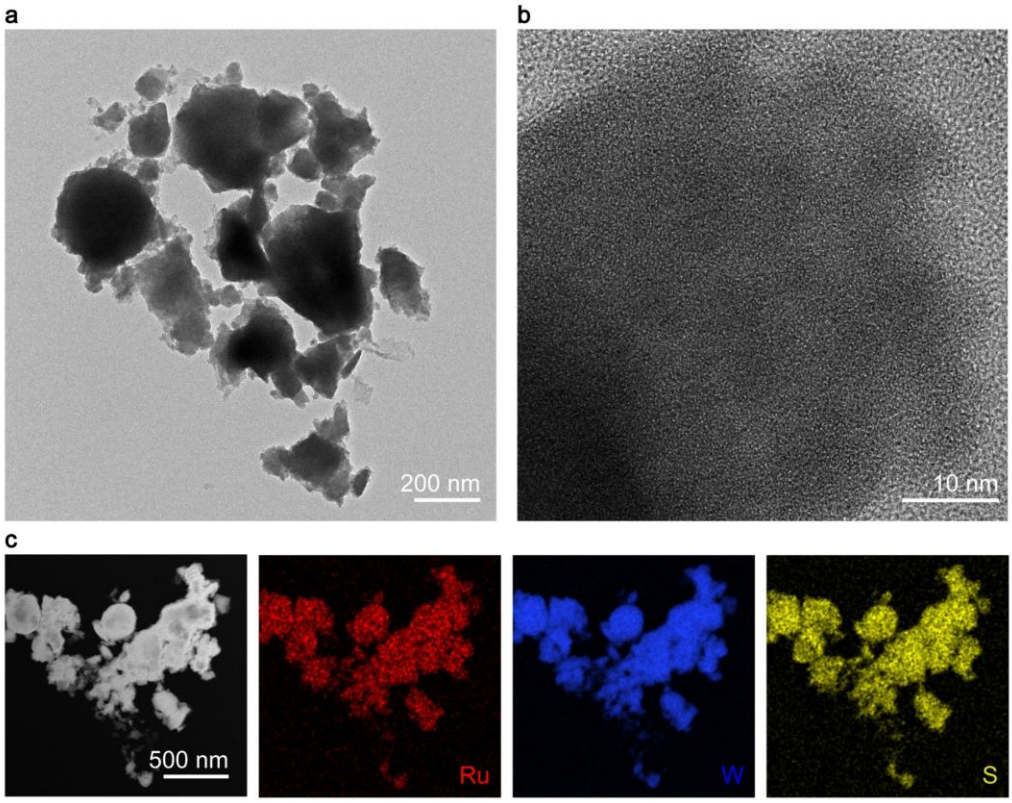

Fig. S19. RuWS powder formed after pyrolysis at 300 °C (denoted as RuWS-300). (a) TEM, (b) HRTEM, and (c) HAADF-STEM and elemental mapping images of RuWS-300.

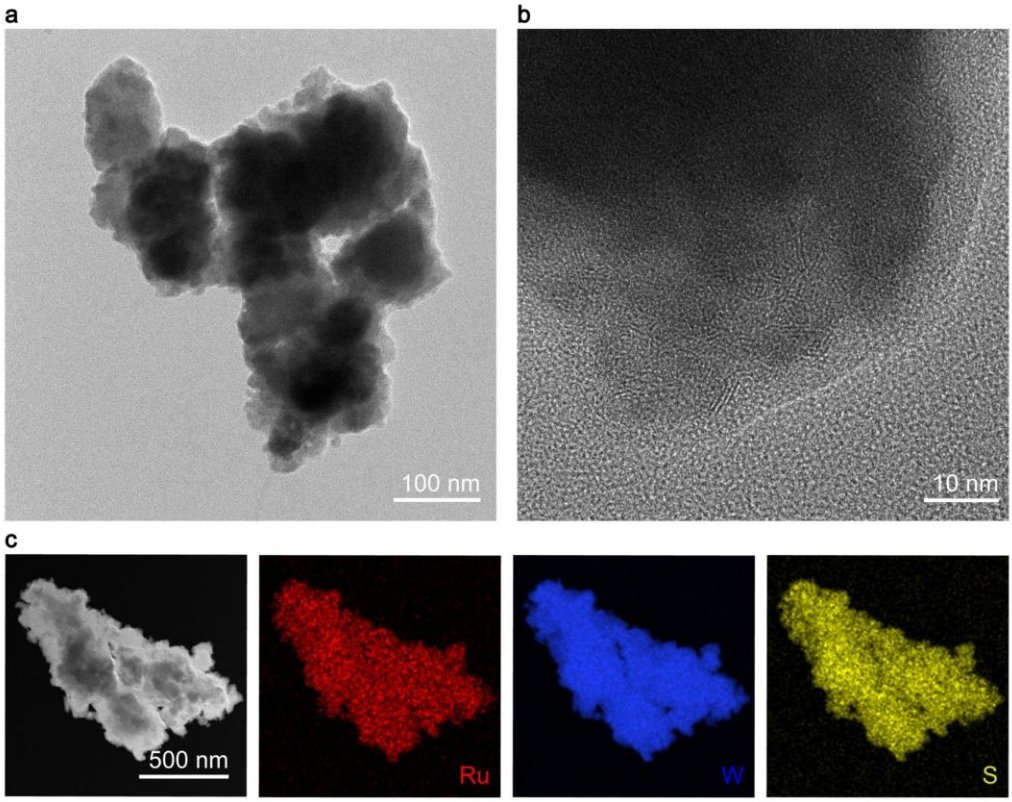

Fig. S20. RuWS powder formed after pyrolysis at 400 °C (denoted as RuWS-400). (a) TEM, (b) HRTEM, and (c) HAADF-STEM and elemental mapping images of RuWS-400.

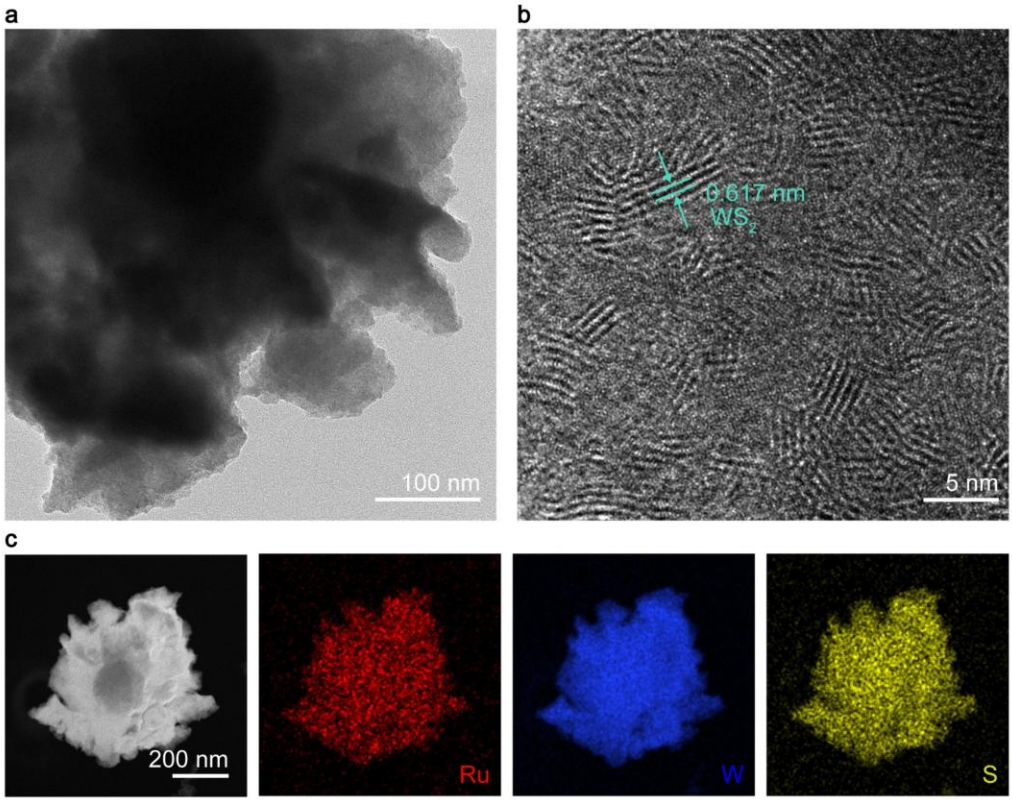

Fig. S21. RuWS powder formed after pyrolysis at 500 °C (denoted as RuWS-500). (a) TEM, (b) HRTEM, and (c) HAADF-STEM and elemental mapping images of RuWS-500.

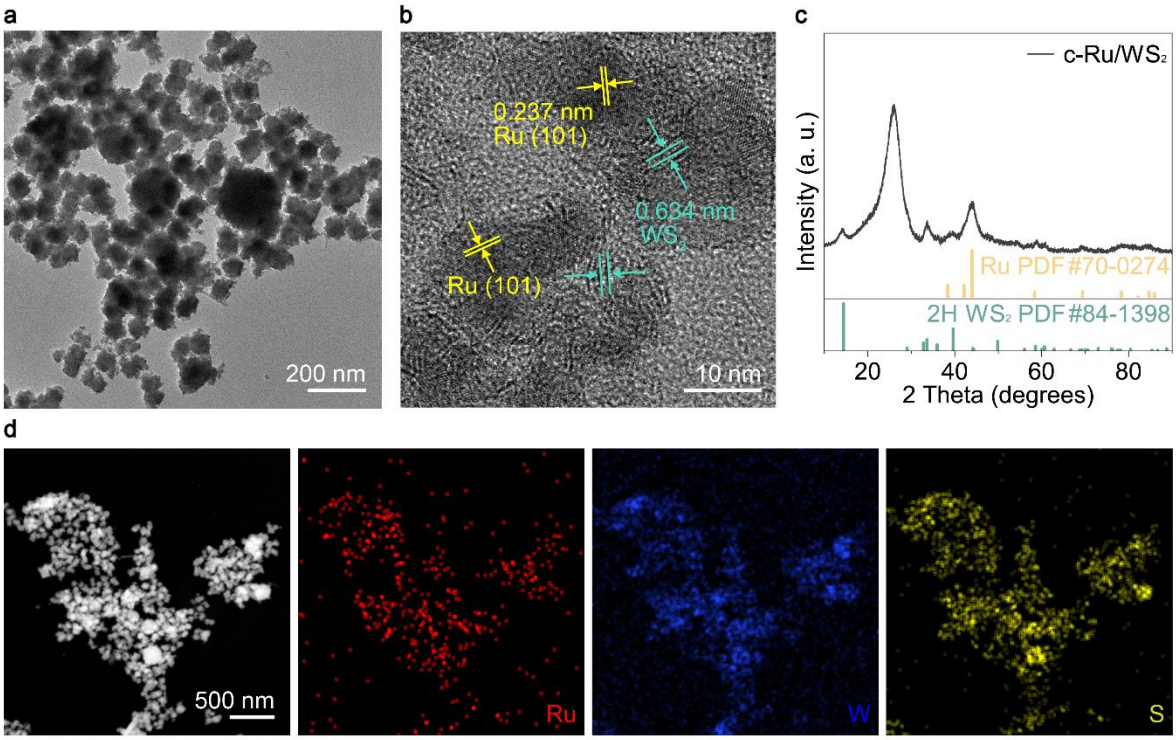

Fig. S22. RuWS powder formed after pyrolysis at 600 ℃**.** (a) TEM, (b) HRTEM, (c) XRD pattern, and (d) HAADF-STEM and elemental mapping images of RuWS powder with crystalline WS_2 and Ru nanoparticles (denoted as c-Ru/WS_2) formed after pyrolysis at 600 ℃.

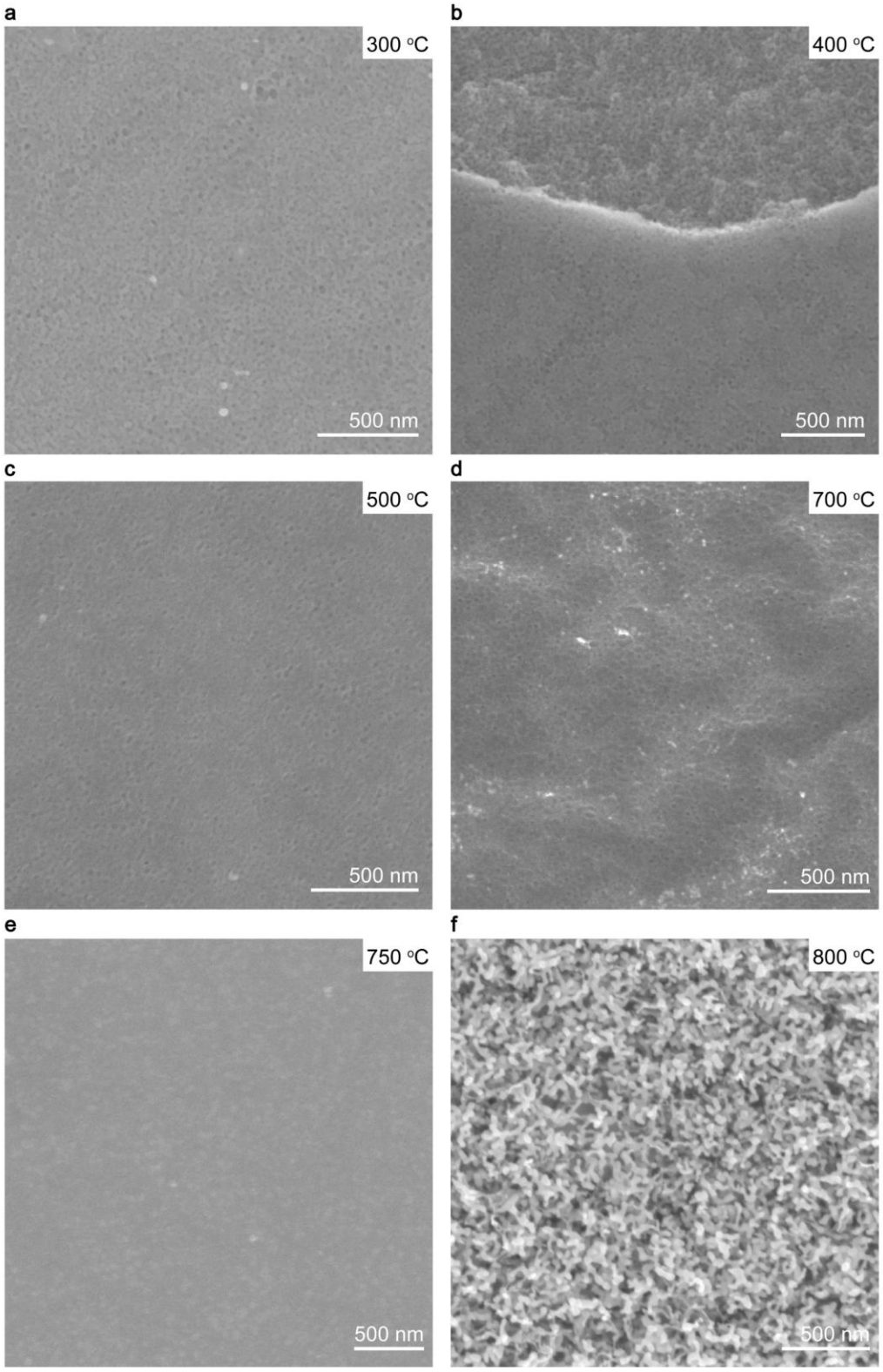

Fig. S23. Morphology of RuWS-accumulated PS-*b*-P2VP micellar film after pyrolysis at different temperatures. SEM images of the samples formed after pyrolysis at (a) 300, (b) 400, (c) 500, (d) 700, (e) 750, and (f) 800 ℃.

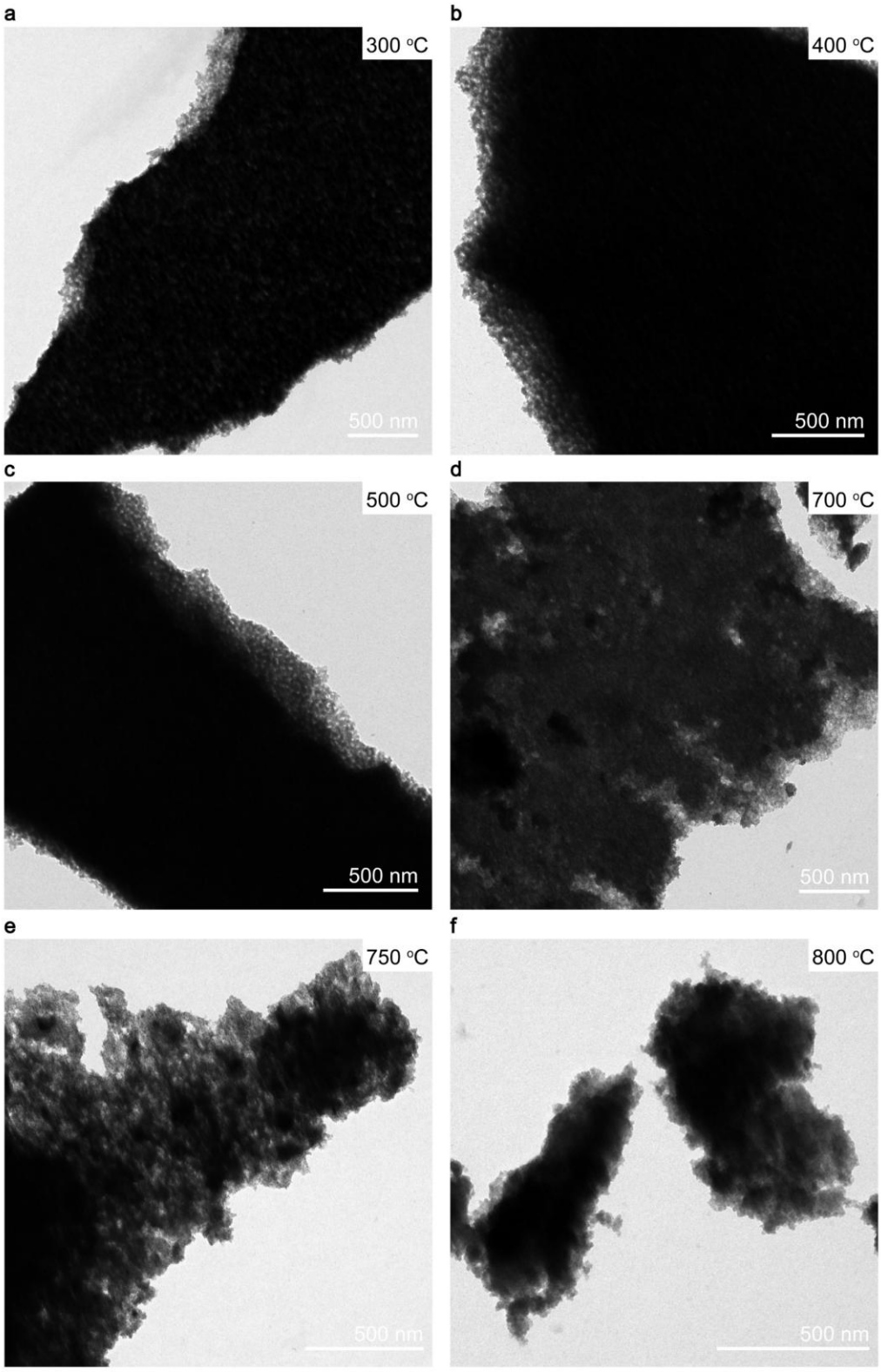

Fig. S24. Structure of RuWS-accumulated PS-*b*-P2VP micellar film after pyrolysis at different temperatures. TEM images of the samples formed after pyrolysis at (a) 300, (b) 400, (c) 500, (d) 700, (e) 750, and (f) 800 °C.

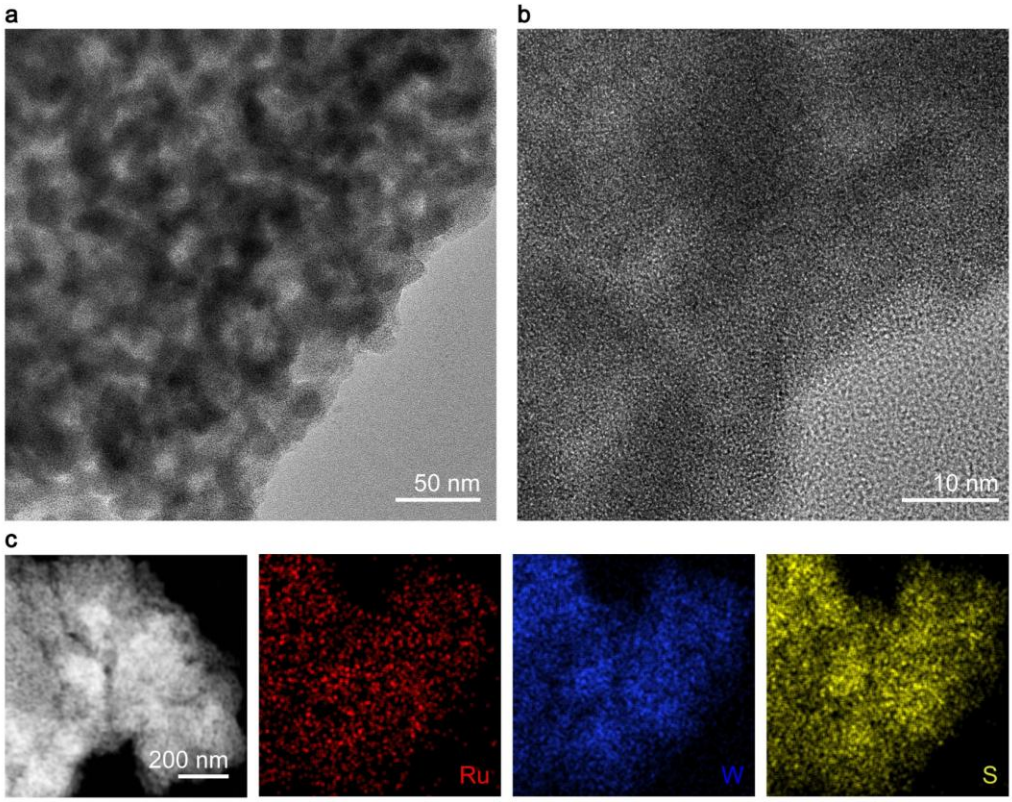

Fig. S25. RuWS-accumulated PS-*b*-P2VP micellar film after pyrolysis at 300 °C (denoted as SV@RuWS-300). (a) TEM, (b) HRTEM, and (c) HAADF-STEM and elemental mapping images of SV@RuWS-300.

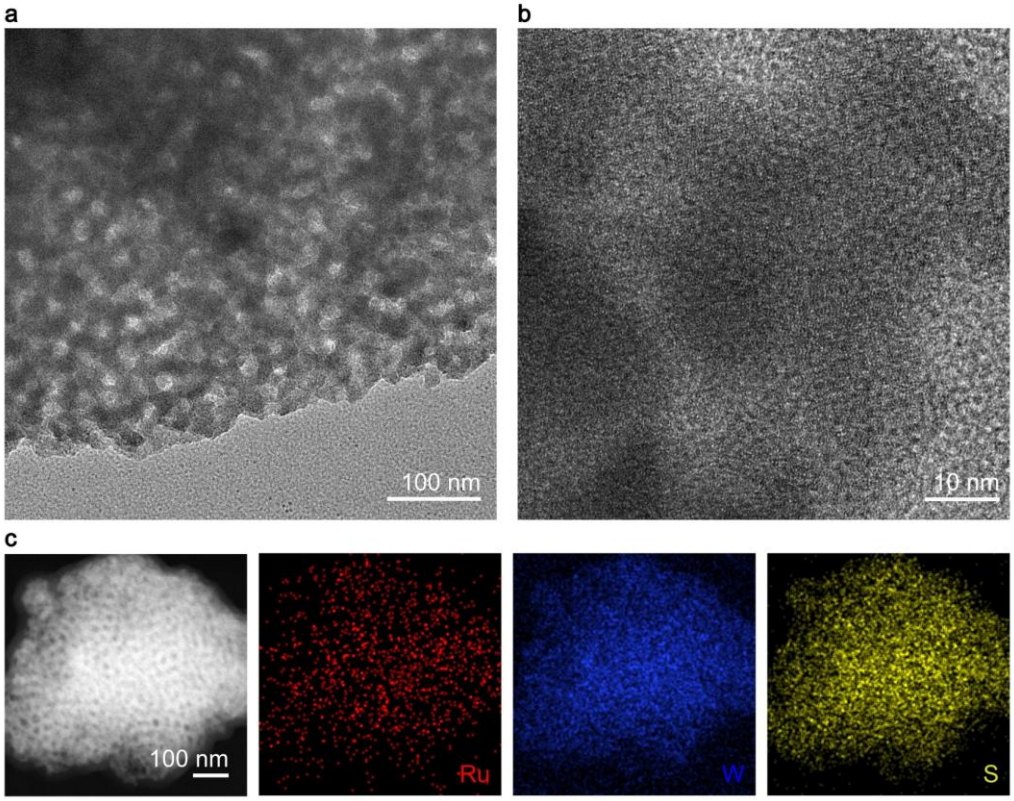

Fig. S26. RuWS-accumulated PS-*b*-P2VP micellar film after pyrolysis at 400 °C (denoted as SV@RuWS-400). (a) TEM, (b) HRTEM, and (c) HAADF-STEM and elemental mapping images of SV@RuWS-400.

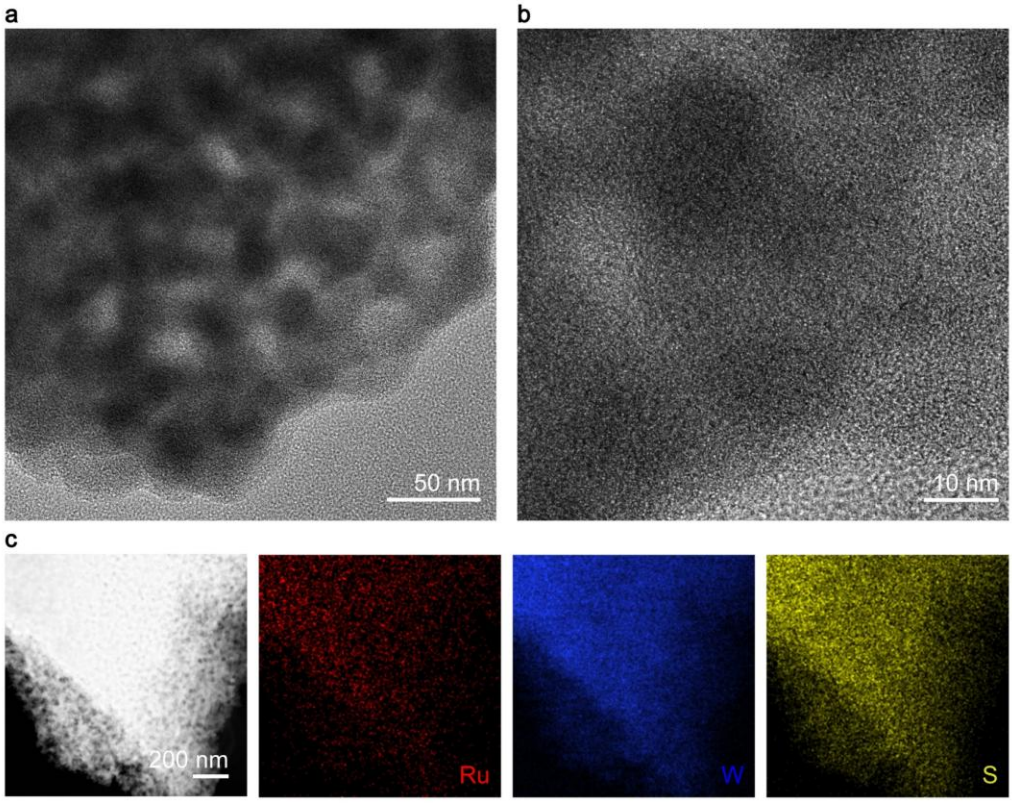

Fig. S27. RuWS-accumulated PS-*b*-P2VP micellar film after pyrolysis at 500 °C (denoted as SV@RuWS-500). (a) TEM, (b) HRTEM, and (c) HAADF-STEM and elemental mapping images of SV@RuWS-500.

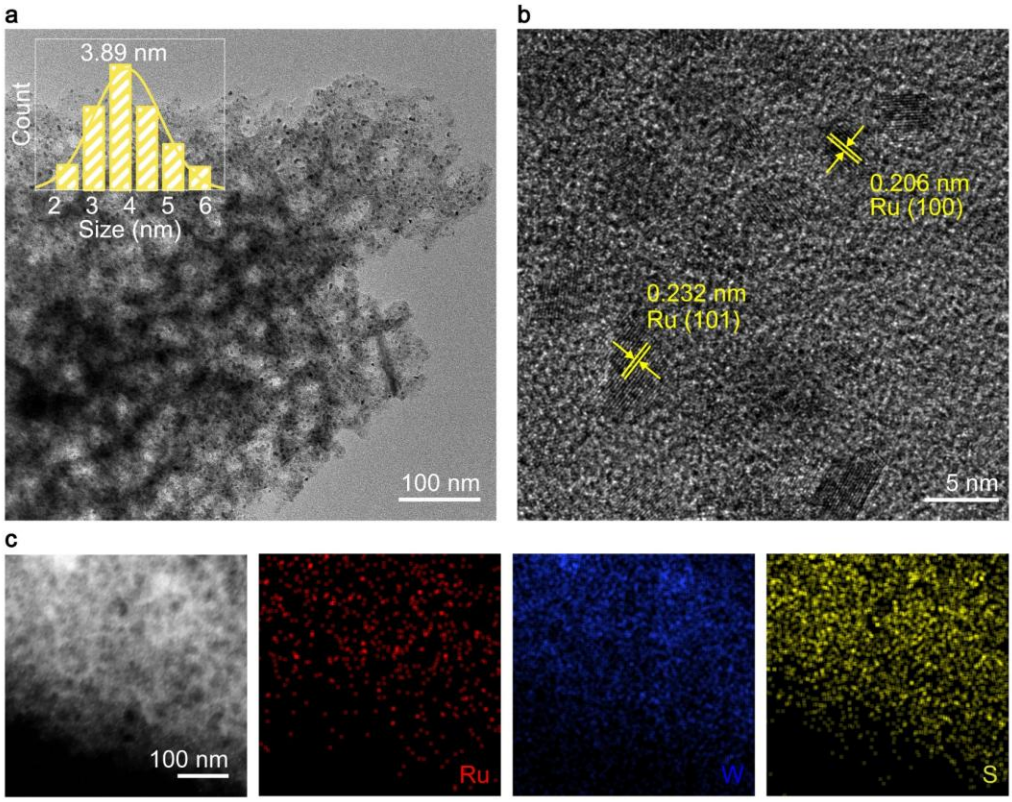

Fig. S28. RuWS-accumulated PS-*b*-P2VP micellar film after pyrolysis at 700 °C (denoted as SV@RuWS-700). (a) TEM, (b) HRTEM, and (c) HAADF-STEM and elemental mapping images of SV@RuWS-700.

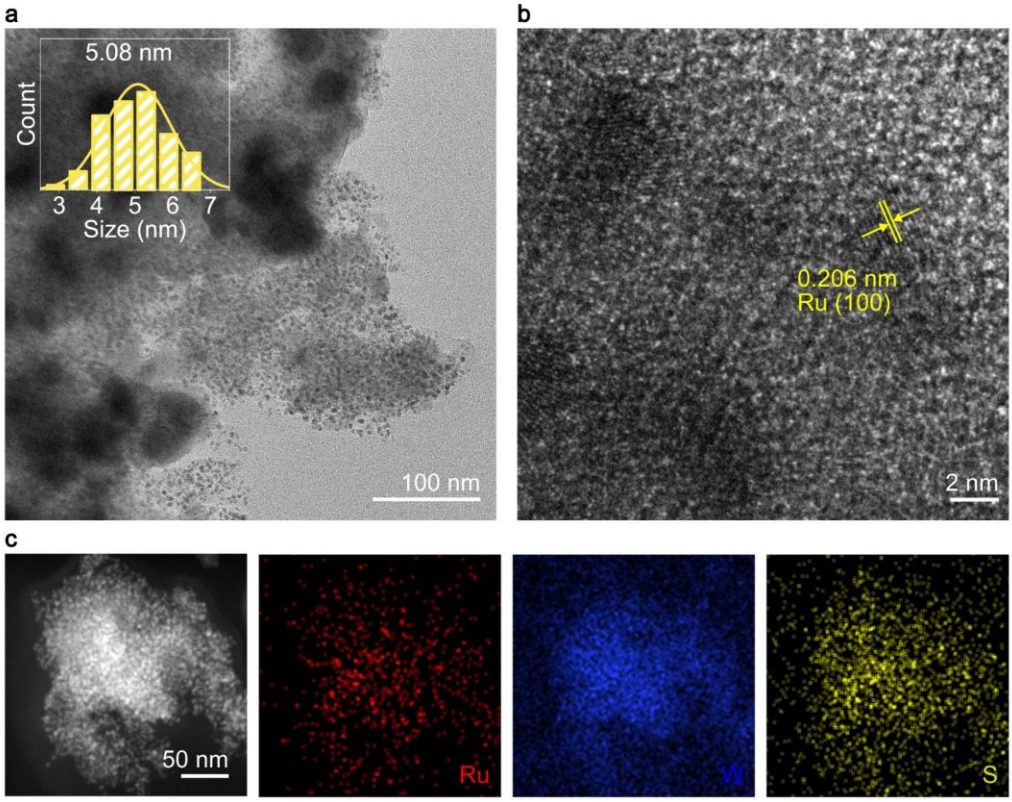

Fig. S29. RuWS-accumulated PS-*b*-P2VP micellar film after pyrolysis at 750 °C (denoted as SV@RuWS-750). (a) TEM, (b) HRTEM, and (c) HAADF-STEM and elemental mapping images of SV@RuWS-750.

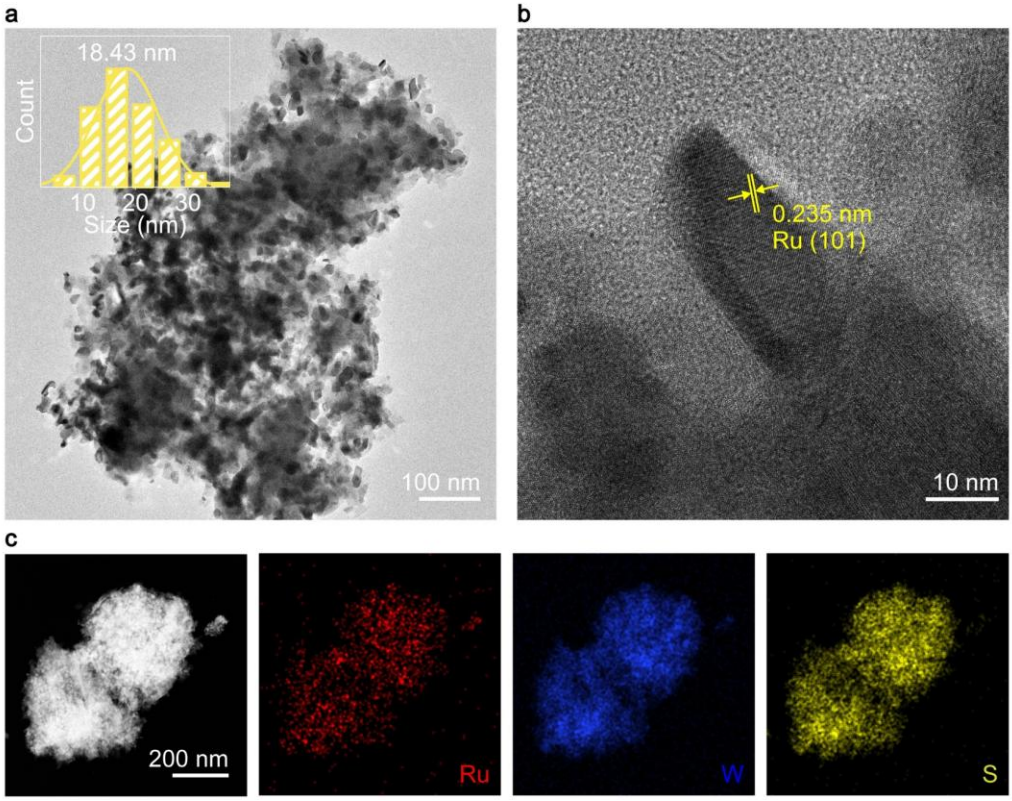

Fig. S30. RuWS-accumulated PS-*b*-P2VP micellar film after pyrolysis at 800 °C (denoted as SV@RuWS-800). (a) TEM, (b) HRTEM, and (c) HAADF-STEM and elemental mapping images of SV@RuWS-800.

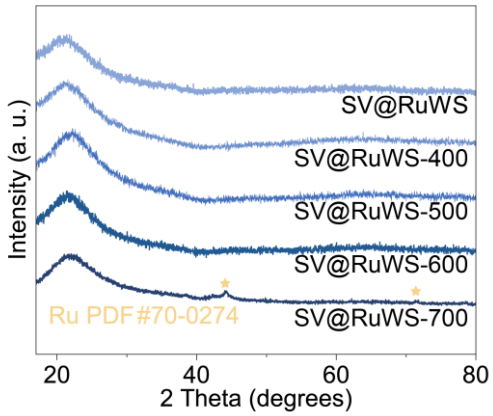

Fig. S31. XRD analysis of RuWS-accumulated micellar film and the samples formed after pyrolysis at different temperatures. XRD pattern of RuWS-accumulated micellar film and the derived samples formed after pyrolysis at 400, 500, 600, and 700 ℃ (denoted as SV@RuWS, SV@RuWS-400, SV@RuWS-500, SV@RuWS-600, and SV@RuWS-700, respectively).

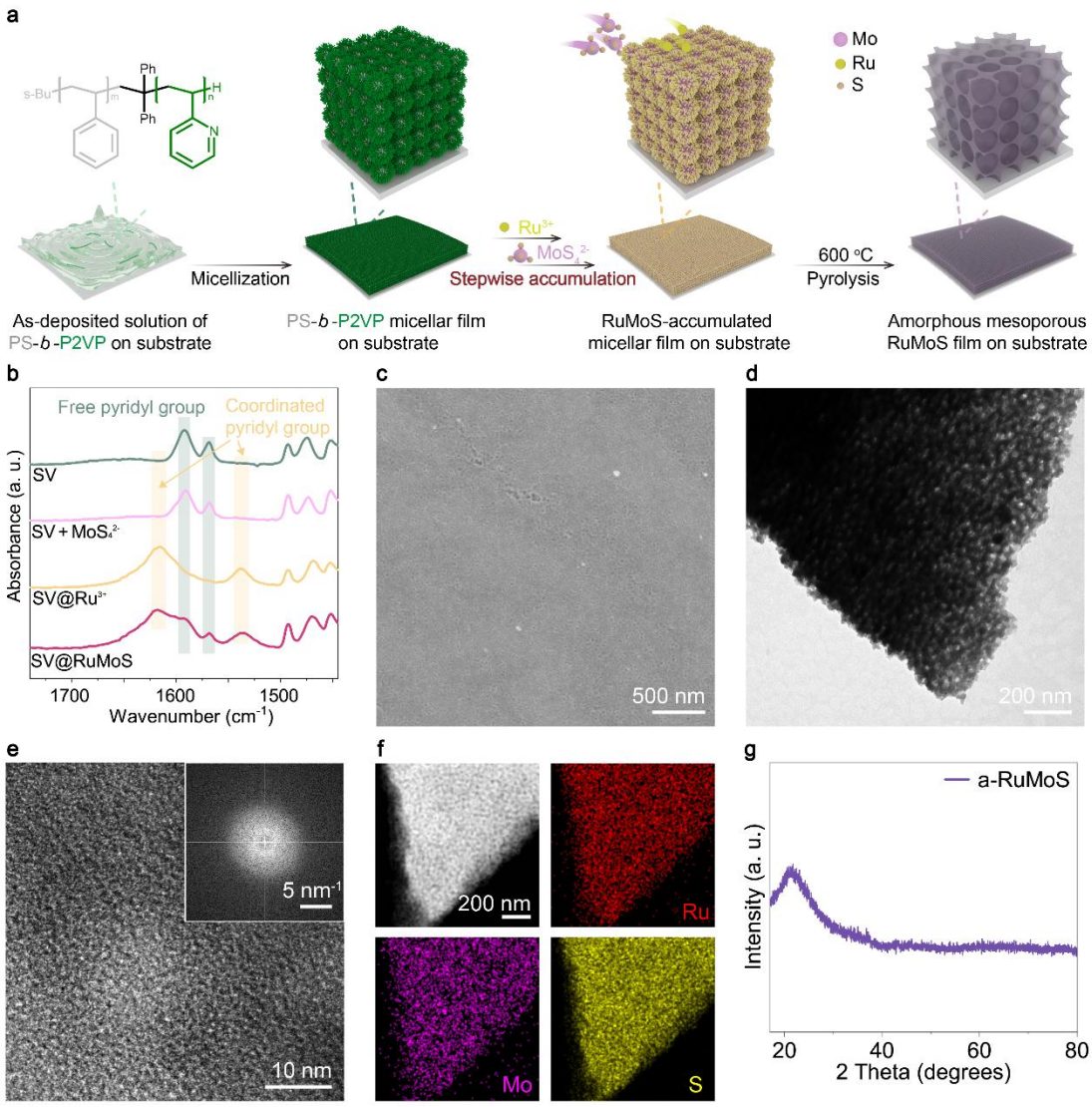

Fig. S32 Amorphous mesoporous RuMoS film. (a) Schematic illustration the fabrication process of amorphous mesoporous RuMoS film. (b) FT-IR spectra of PS-*b*-P2VP micellar film, PS-*b*-P2VP micellar film after immersing in a solution of MoS_4^{2-} ions in ethanol, Ru^{3+} ion-accumulated PS-*b*-P2VP micellar film, and RuWS-accumulated PS-*b*-P2VP micellar film (denoted as SV, SV+MoS_4^{2-}, SV@Ru^{3+}, and SV@RuMoS, respectively). (c) SEM, (d) TEM, (e) HRTEM (insert is the corresponding FFT image with characteristic weak diffusion ring), and (f) HAADF-STEM and elemental mapping images of amorphous mesoporous RuMoS film. (g) XRD pattern of amorphous mesoporous RuMoS film.

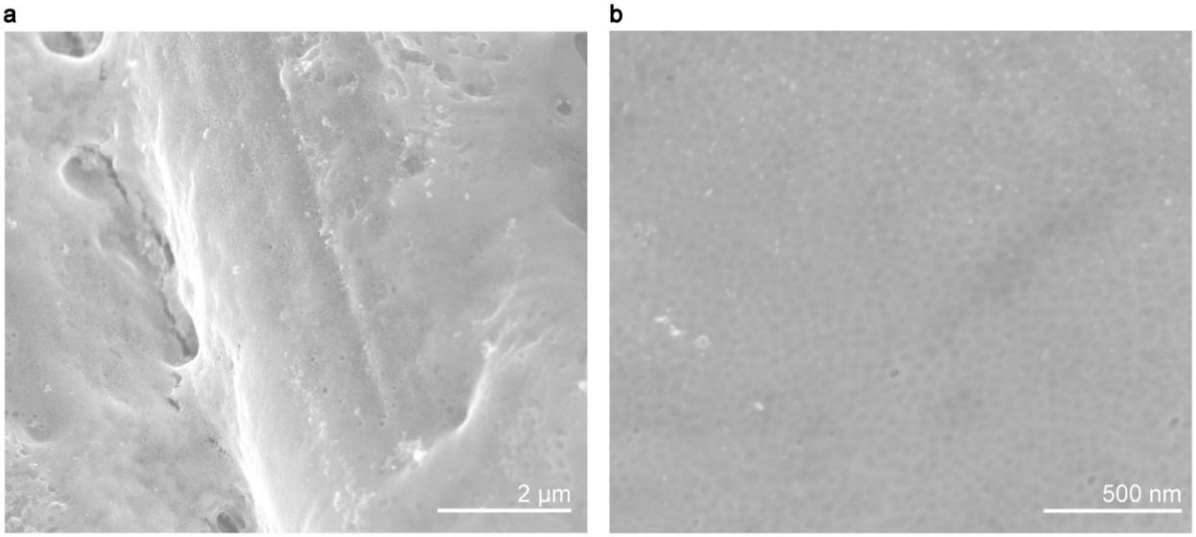

Fig. S33. Amorphous mesoporous RuWS film on carbon cloth electrode. SEM images of amorphous mesoporous RuWS film on carbon cloth formed by pyrolysis of the RuWS-accumulated micellar film at 600 ℃.

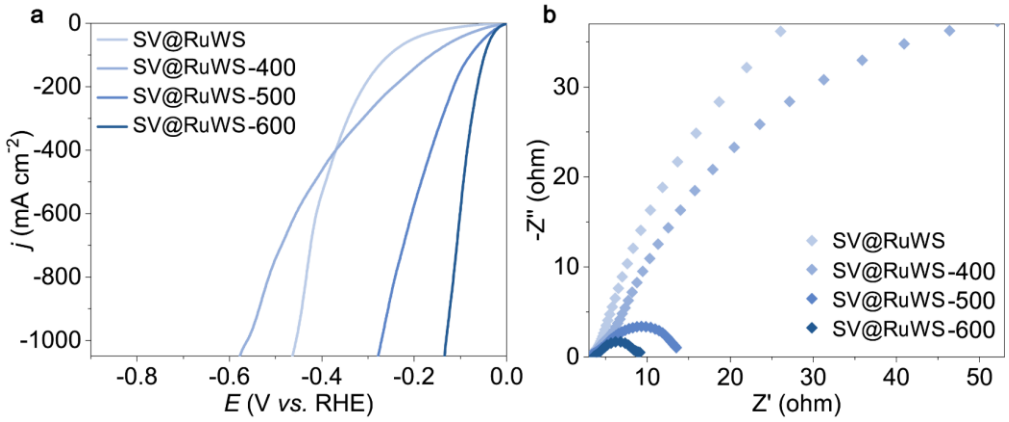

Fig. S34. Electrochemical HER performances of RuWS-accumulated PS-*b*-P2VP micellar film and the samples formed after pyrolysis at different temperatures. (a) HER LSV curves with iR-correction and (b) EIS Nyquist plots for HER of RuWS-accumulated micellar film and the derived samples formed after pyrolysis at 400, 500 and 600 ℃ (denoted as SV@RuWS, SV@RuWS-400, SV@RuWS-500 and SV@RuWS-600, respectively).

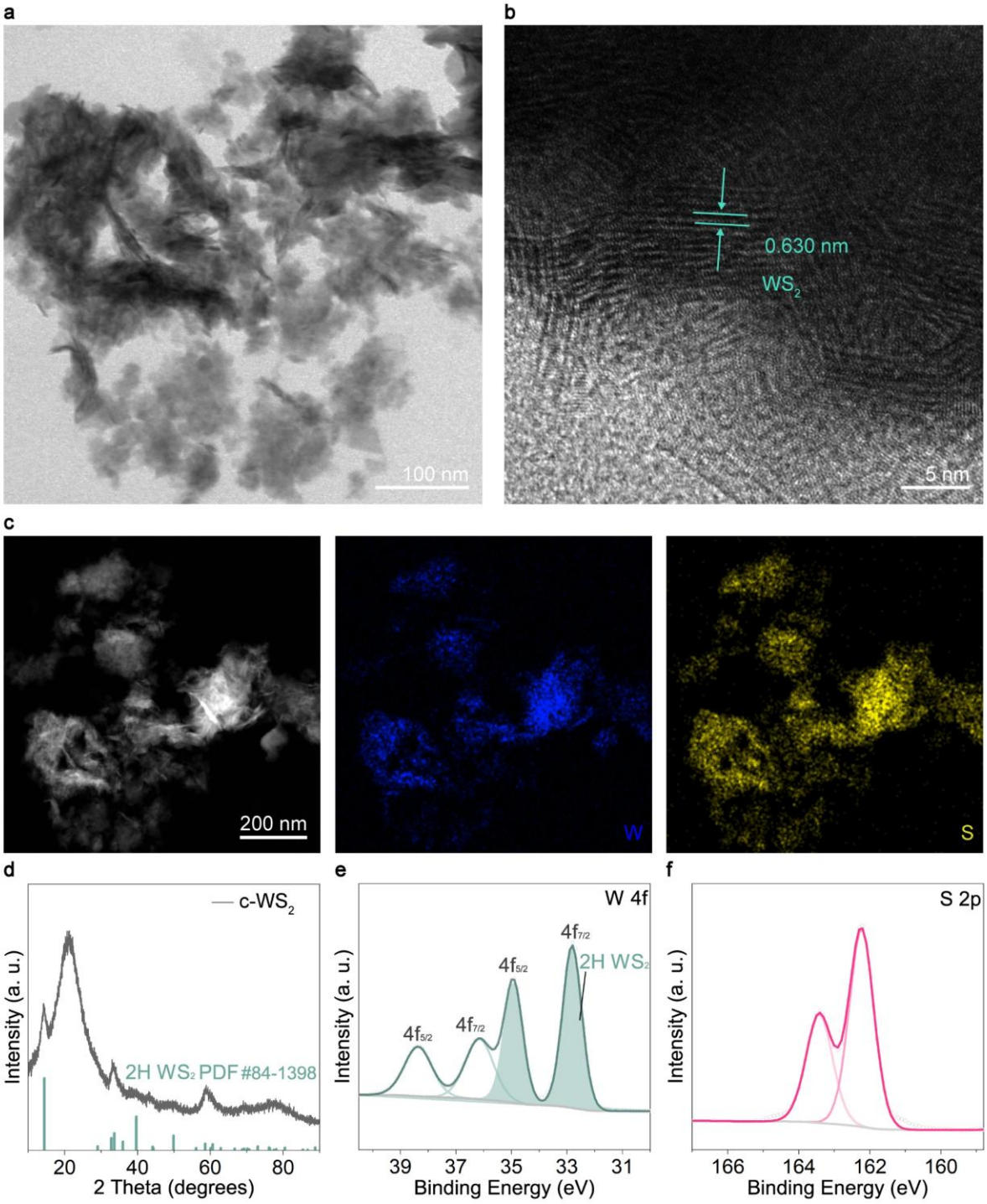

Fig. S35. $(NH_4)_2WS_4$ powder after pyrolysis at 600 °C. (a) TEM, (b) HRTEM, (c) HAADF-STEM and elemental mapping images, (d) XRD pattern, and (e, f) high-resolution XPS spectra of (e) W 4f and (f) S 2p of the sample with crystalline WS_2 (denoted as c-WS_2) formed by pyrolysis of the $(NH_4)_2WS_4$ powder at 600 ℃.

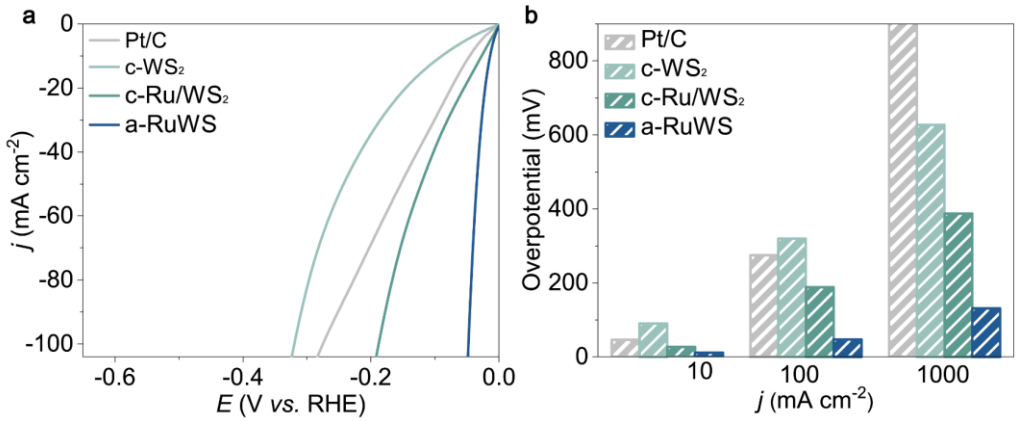

Fig. S36. Electrochemical HER performances. (a) HER LSV curves with iR-correction and (b) overpotential at different current densities of commercial Pt/C, crystalline WS_2 (denoted as c-WS_2), crystalline WS_2 with Ru nanoparticles (denoted as c-Ru/WS_2), and amorphous mesoporous RuWS film (denoted as a-RuWS).

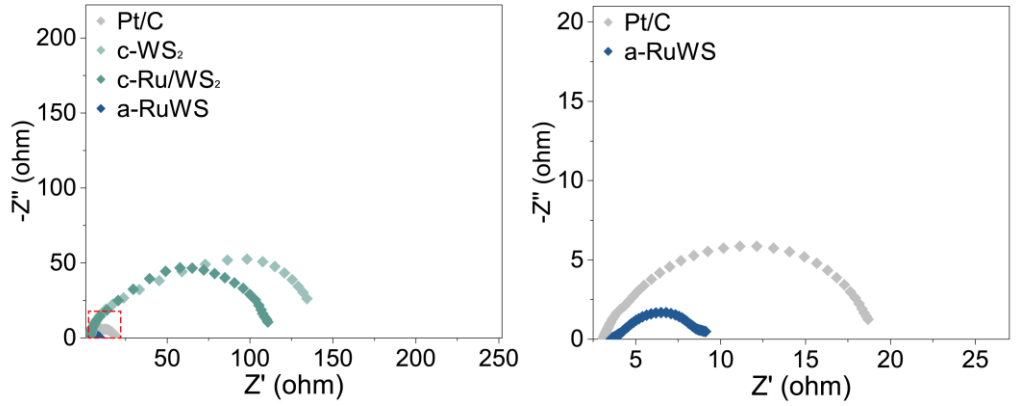

Fig. S37. Electrochemical test for EIS. EIS Nyquist plots of commercial Pt/C, crystalline WS_2 (denoted as c-WS_2), crystalline WS_2 with Ru nanoparticles (simply denoted as c-Ru/WS_2), and amorphous mesoporous RuWS film (denoted as a-RuWS) in an aqueous solution of 1.0 M KOH.

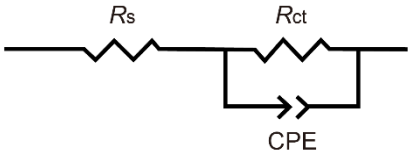

Fig. S38. Electrical equivalent circuit of amorphous mesoporous RuWS film.

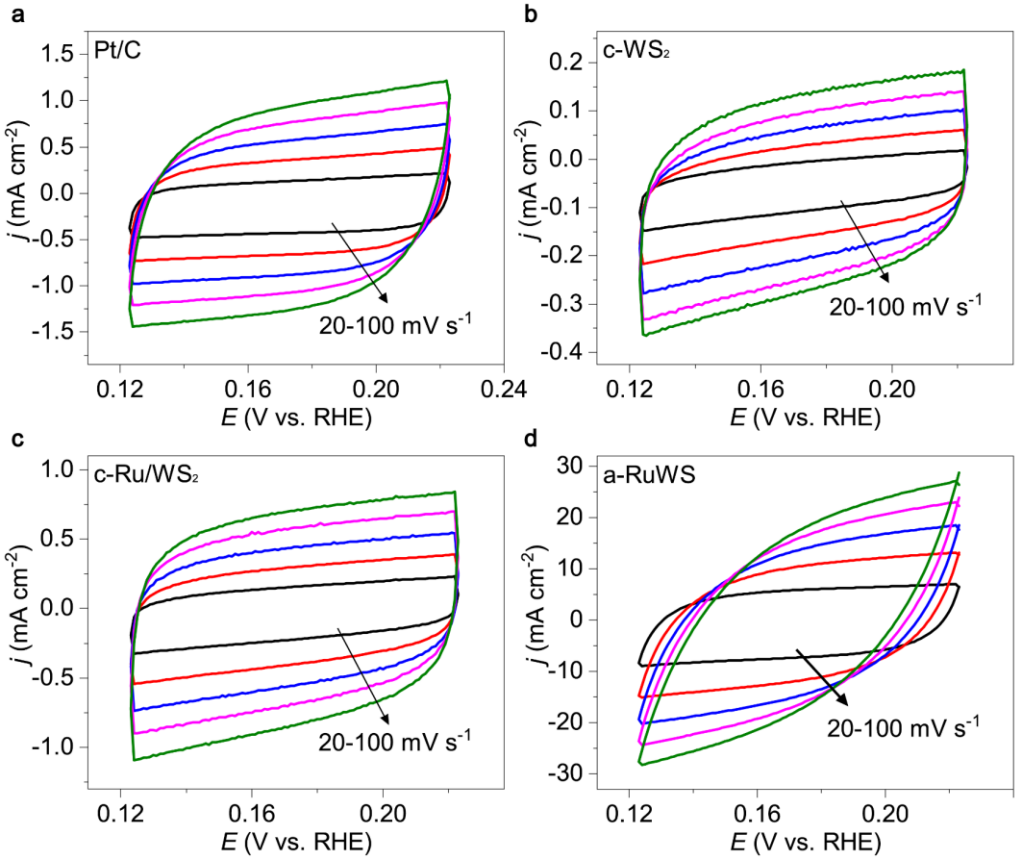

Fig. S39. Electrochemical test for C_{dl}. CV curves of (a) commercial Pt/C, (b) crystalline WS_2 (simply denoted as c-WS_2), (c) crystalline WS_2 with Ru nanoparticles (denoted as c-Ru/WS_2), and (d) amorphous mesoporous RuWS film (denoted as a-RuWS) at increasing scan rates of 20–100 mV s^{-1} in 1.0 M KOH.

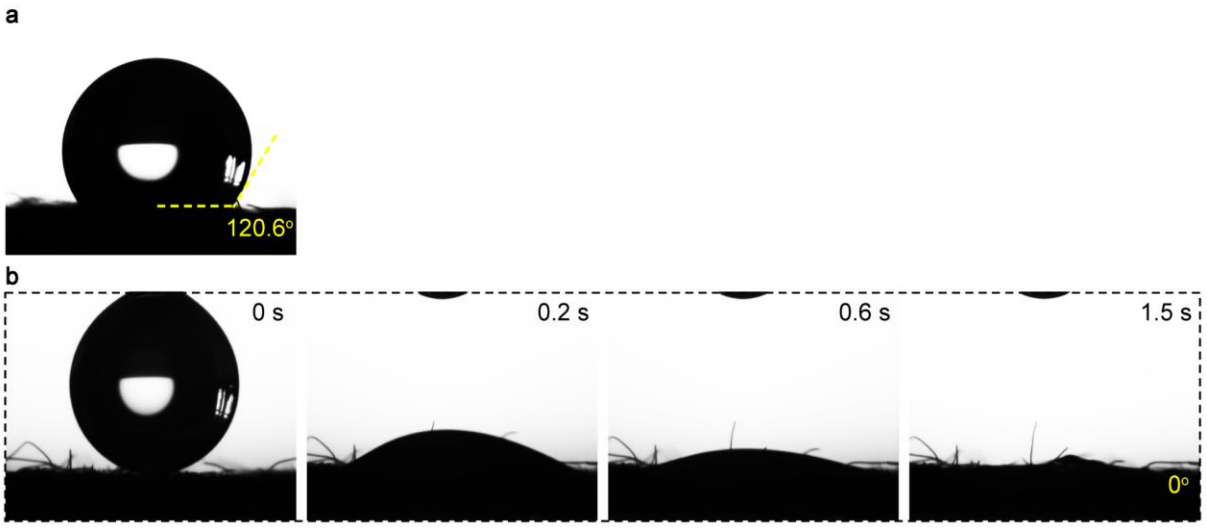

Fig. S40. Hydrophilicity test. Contact angles of (a) bare carbon cloth and (b) amorphous mesoporous RuWS film-decorated carbon cloth.

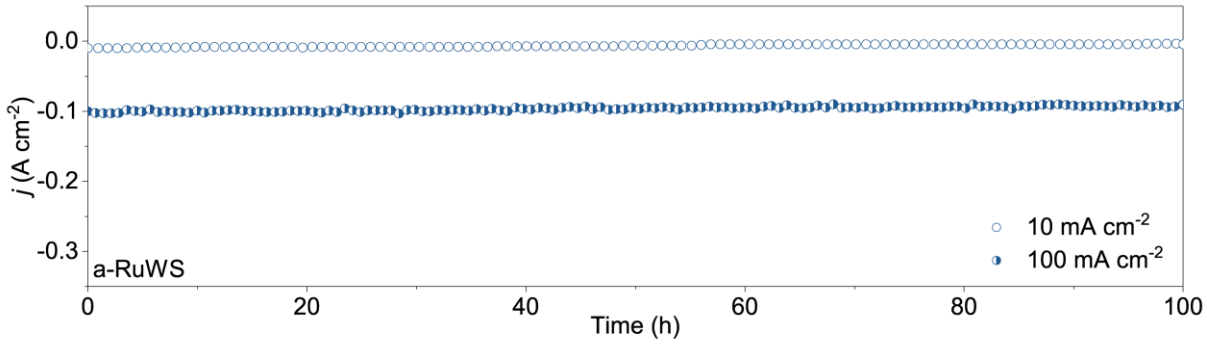

Fig. S41. Electrochemical stability test. Chronoamperometry curves of amorphous mesoporous RuWS film (denoted as a-RuWS) at 10 and 100 mA cm^{-2}, respectively.

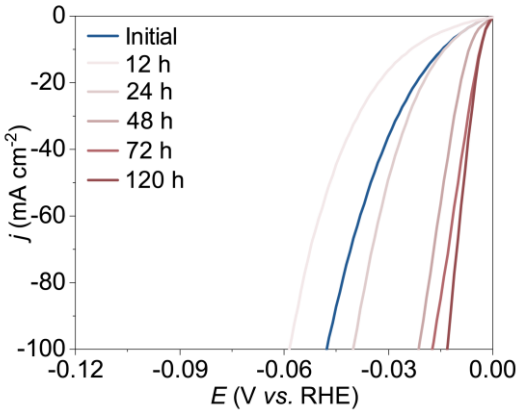

Fig. S42. Evolution of electrochemical HER performances. HER LSV curves of amorphous mesoporous RuWS film before and after HER stability test.

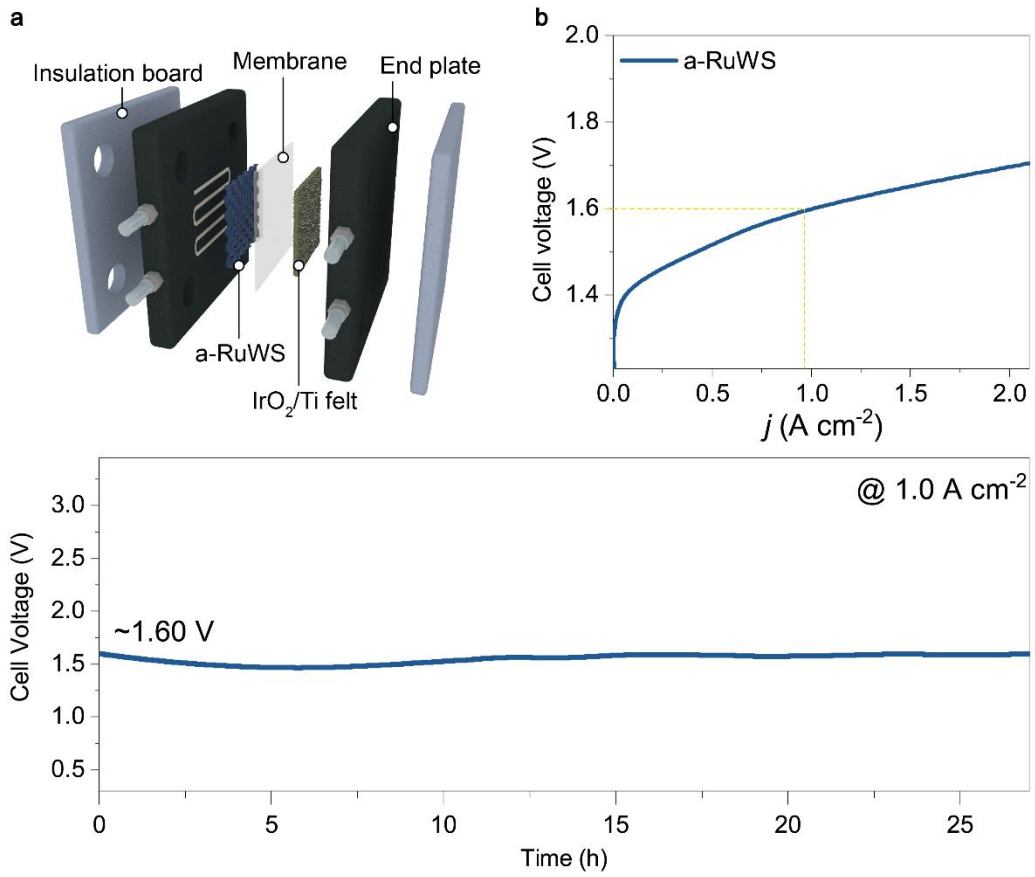

Fig. S43. AEMWE performance of amorphous mesoporous RuWS film. (a) Schematic diagram of a AEMWE device. (g) Polarization curves of AEMWEs assembled using the amorphous mesoporous RuWS film and commercial IrO_2. (h) Durability of the AEMWE at current density of 1.0 A cm^{-2}.

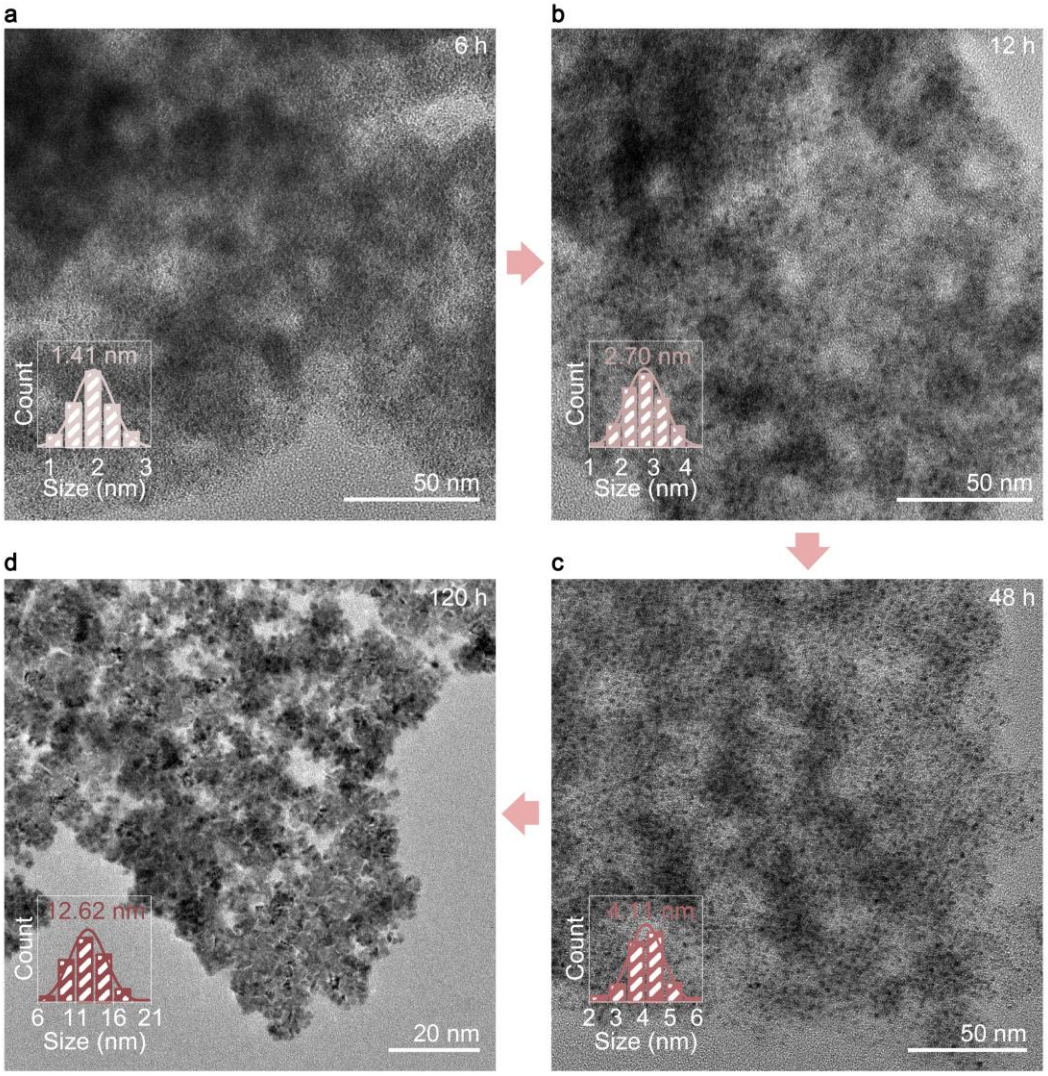

Fig. S44. Generation of crystalline nanoparticles during electrochemical test. TEM images of amorphous mesoporous RuWS film acquired at 6 h, 12 d, 48 h, and 120 h during electrochemical test, respectively.

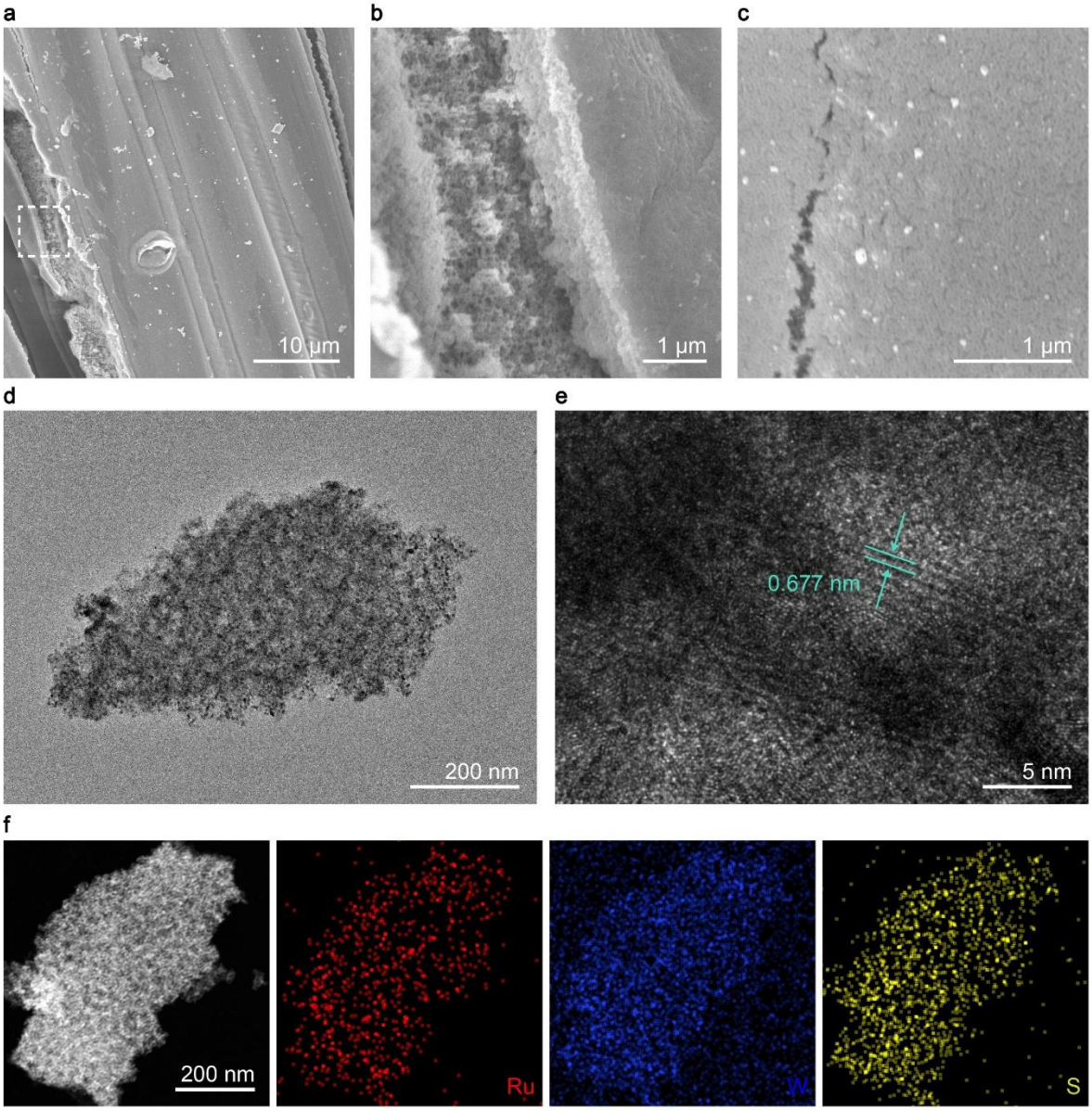

Fig. S45. Amorphous mesoporous RuWS film after stability test. (a−c) TEM, (d) TEM, (e) HRTEM, and (f) HAADF-STEM and elemental mapping images of amorphous mesoporous RuWS film after the electrochemical test.

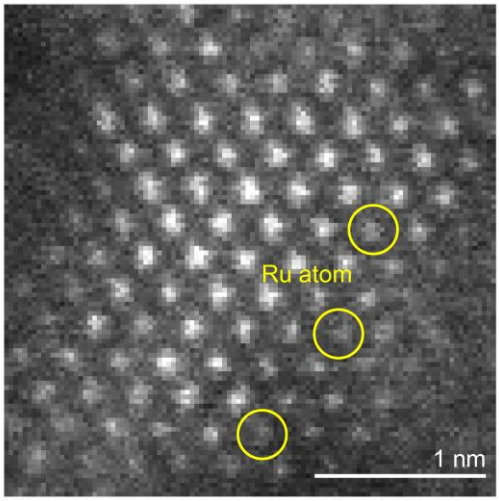

Fig. S46. AC-HAADF-STEM image of amorphous mesoporous RuWS film after the electrochemical test.

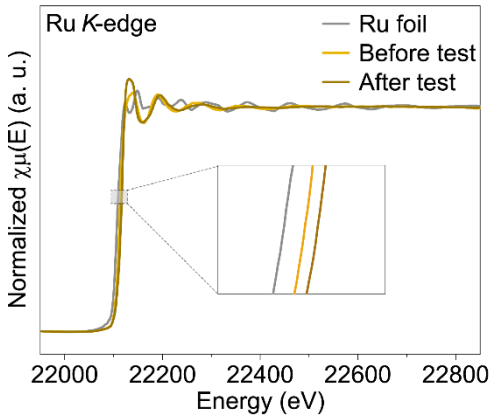

Fig. S47. XANES spectra at Ru *K*-edge of amorphous mesoporous RuWS film before and after the electrochemical test.

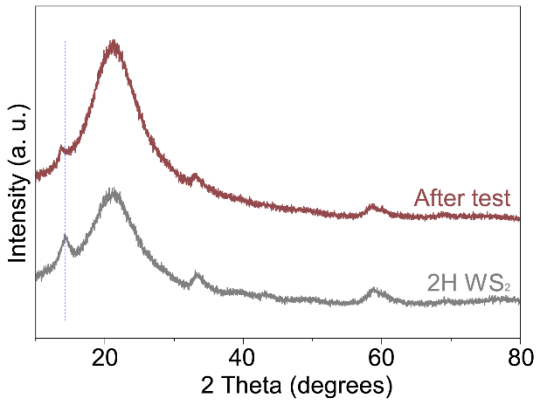

Fig. S48. XRD pattern of the 2H-phase WS_2 and amorphous mesoporous RuWS film after the electrochemical test.

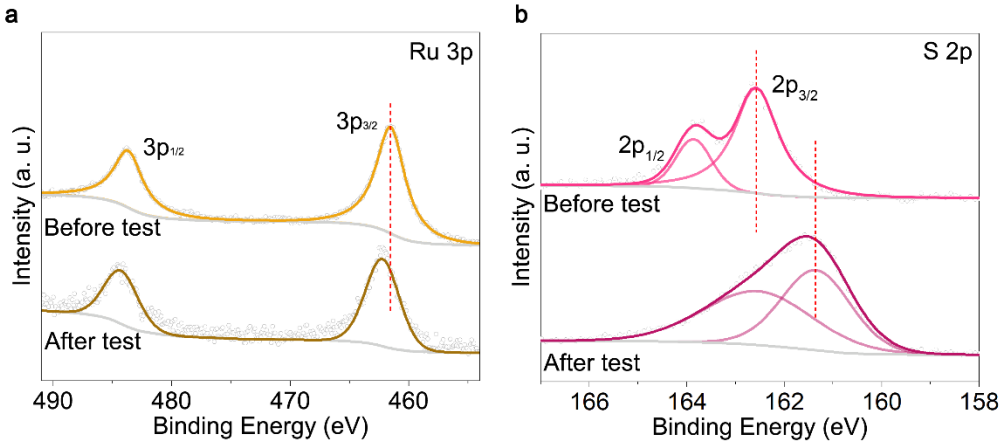

Fig. S49. XPS analysis of amorphous mesoporous RuWS film before and after the electrochemical test. High-resolution XPS spectra of (a) Ru 3p and (b) S 2p of amorphous mesoporous RuWS film before and after the electrochemical test.

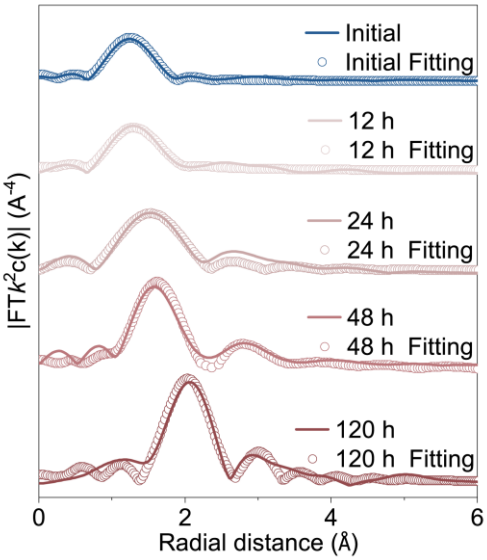

Fig. S50. EXAFS analysis of amorphous mesoporous RuWS film during the electrochemical test. W L_3-edge EXAFS fitting curves at R-space of amorphous mesoporous RuWS film acquired at various periods of the electrochemical test, respectively.

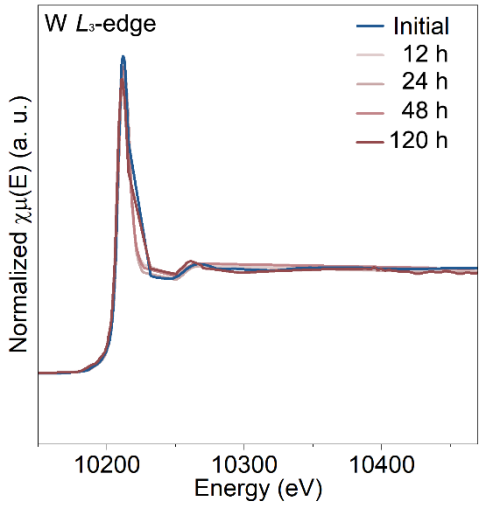

Fig. S51. XANES analysis of amorphous mesoporous RuWS film during the electrochemical test. XANES spectra at W L_3-edge of amorphous mesoporous RuWS film at various periods of the electrochemical test.

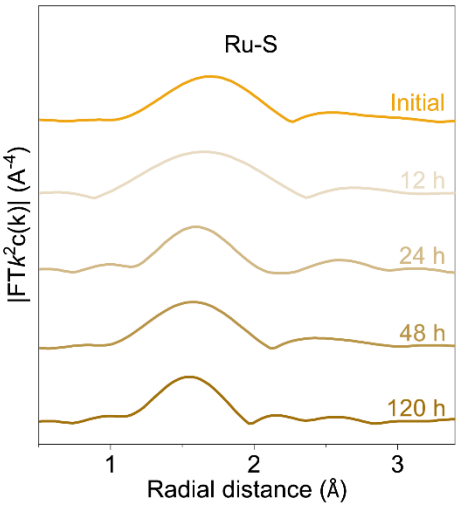

Fig. S52. EXAFS analysis of amorphous mesoporous RuWS film during the electrochemical test. EXAFS spectra at the Ru *K*-edge of amorphous mesoporous RuWS film at various periods of the electrochemical test.

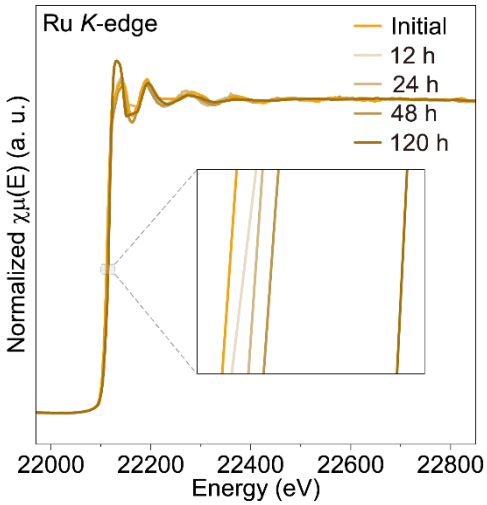

Fig. S53. XANES analysis of amorphous mesoporous RuWS film during the electrochemical test. XANES spectra at Ru *K*-edge of amorphous mesoporous RuWS film at various periods of the electrochemical test.

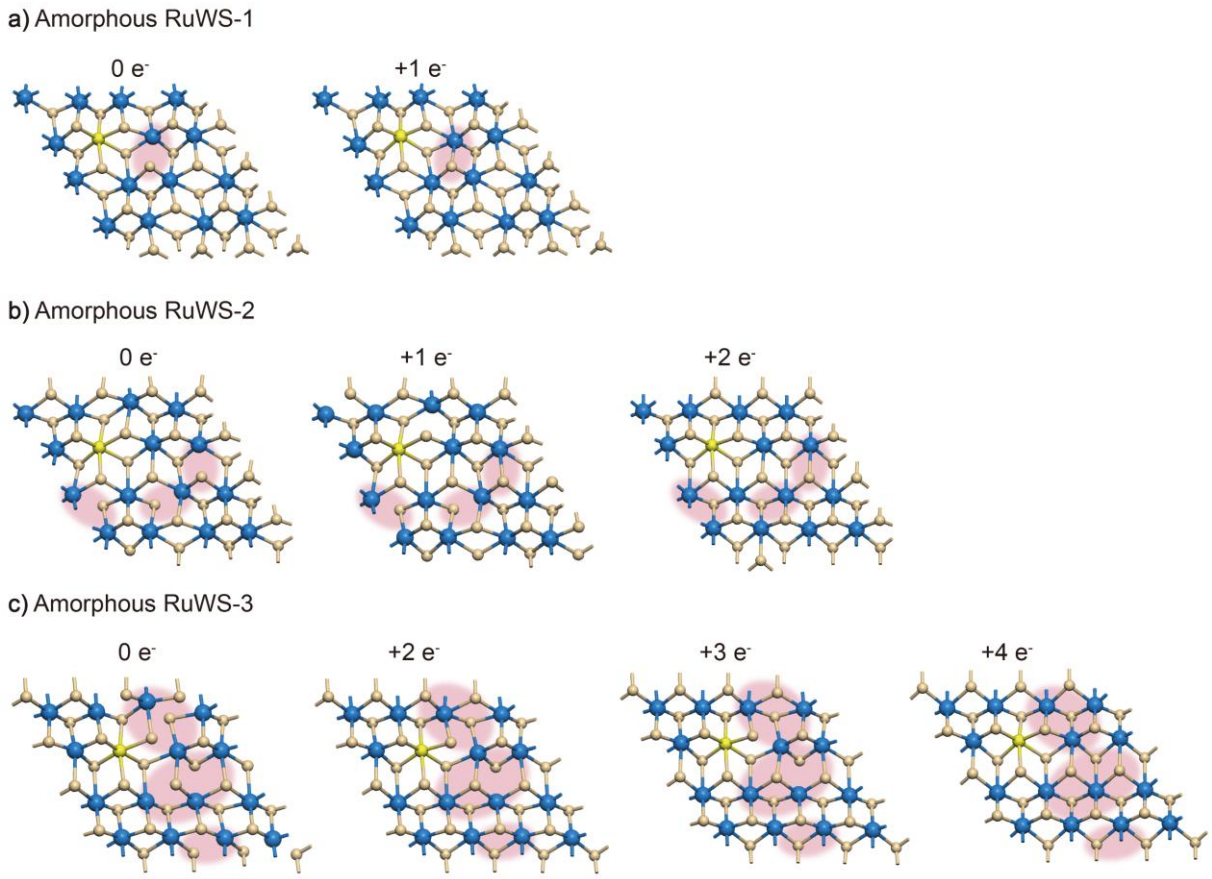

Fig. S54. Three atomic configurations of sulfur-bridged amorphous Ru-W bimetallic composites before and after being injected with increasing number of electrons. (a) amorphous RuWS-1 with minor atomic disorder, (b) amorphous RuWS-2 with partial atomic disorder, and (c) amorphous RuWS-3 with high atomic disorder. The blue, yellow and salmon pink balls represent W, Ru, and S atoms, respectively.

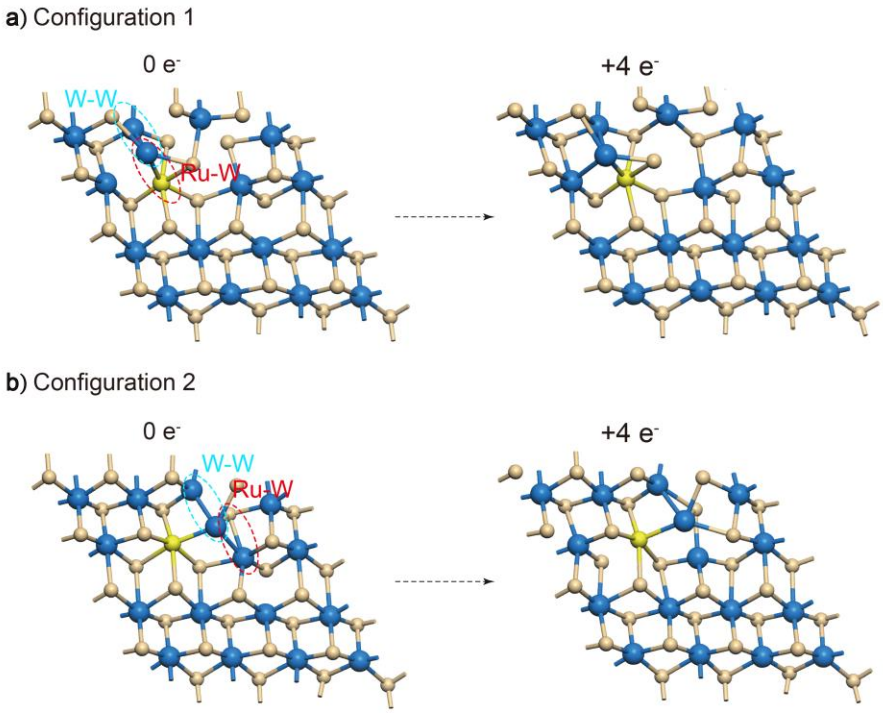

Fig. S55. Two atomic configurations of amorphous Ru-W bimetallic sulfides with Ru-W and W-W bonds (denoted as amorphous RuWS-4) before and after being injected with 4 electrons. The blue, yellow and salmon pink balls represent W, Ru, and S atoms, respectively.

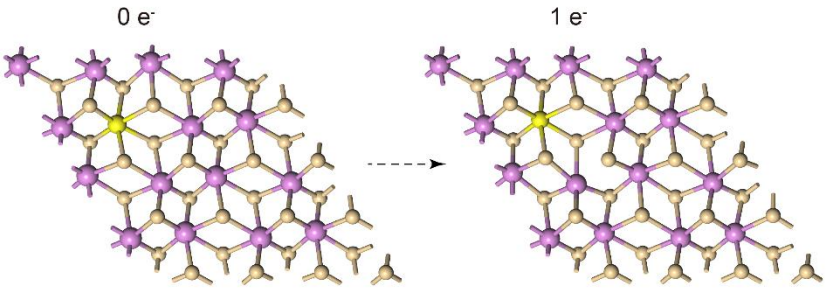

Fig. S56. Configurations of sulfur-bridged amorphous Ru-Mo bimetallic composites before and after being injected with 1 electron. The Pink, yellow and salmon pink balls represent Mo, Ru, and S atoms, respectively.

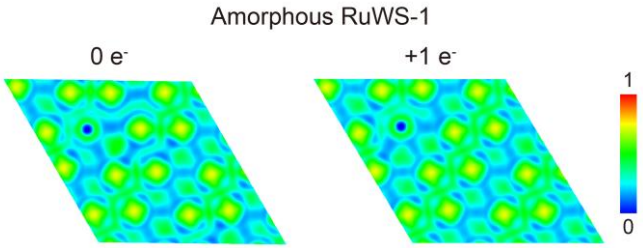

Fig. S57. Variation of electron localization function before and after being injected with 1 electron in amorphous RuWS-1.

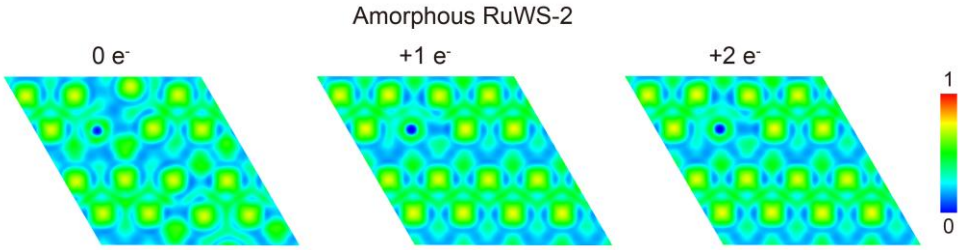

Fig. S58. Variation of electron localization function with increasing number of injected electrons in amorphous RuWS-2.

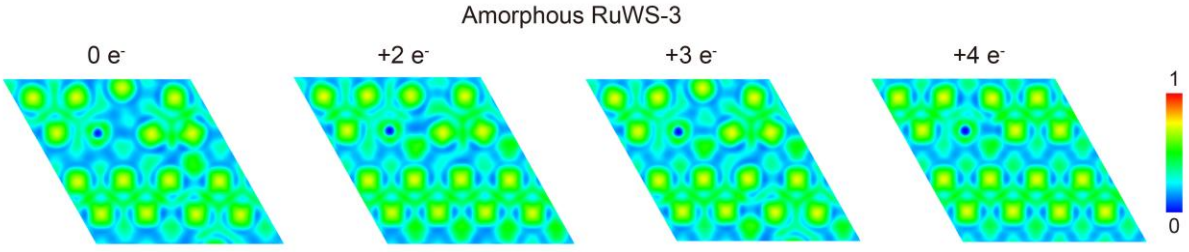

Fig. S59. Variation of electron localization function with increasing number of injected electrons in amorphous RuWS-3.

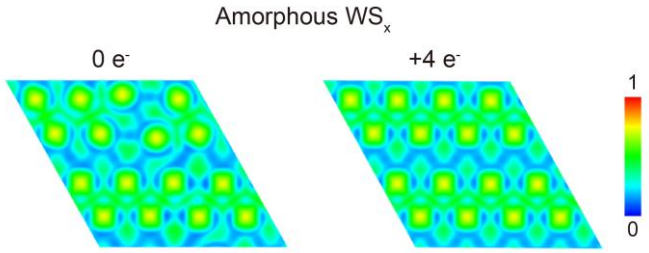

Fig. S60. Variation of electron localization function before and after being injected with 4 electrons in amorphous WS_x.

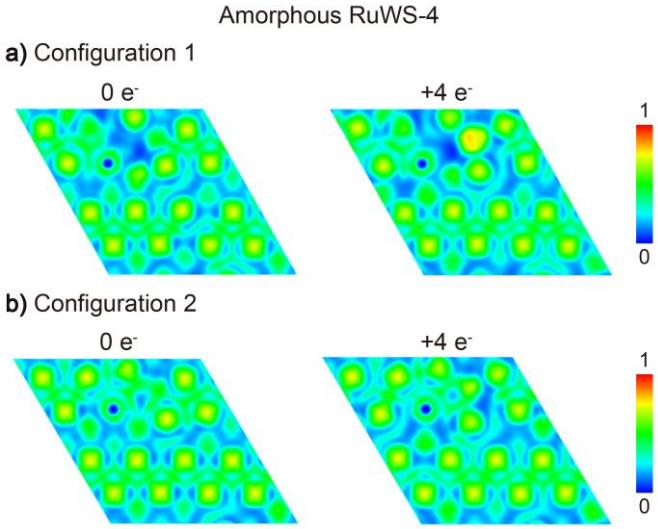

Fig. S61. Variation of electron localization function before and after being injected with 4 electrons in amorphous RuWS-4.

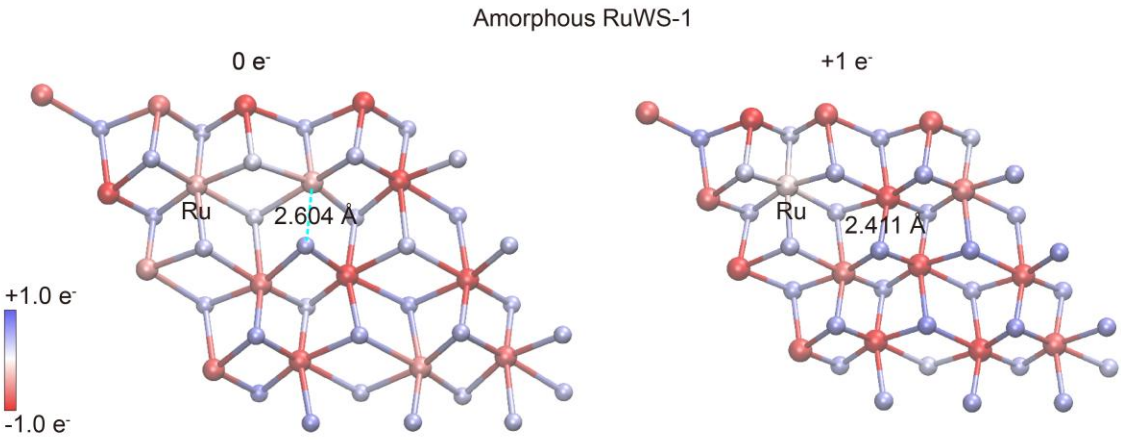

Fig. S62. Bader charge on amorphous RuWS-1 and relevant bond lengths before and after the electron injection.

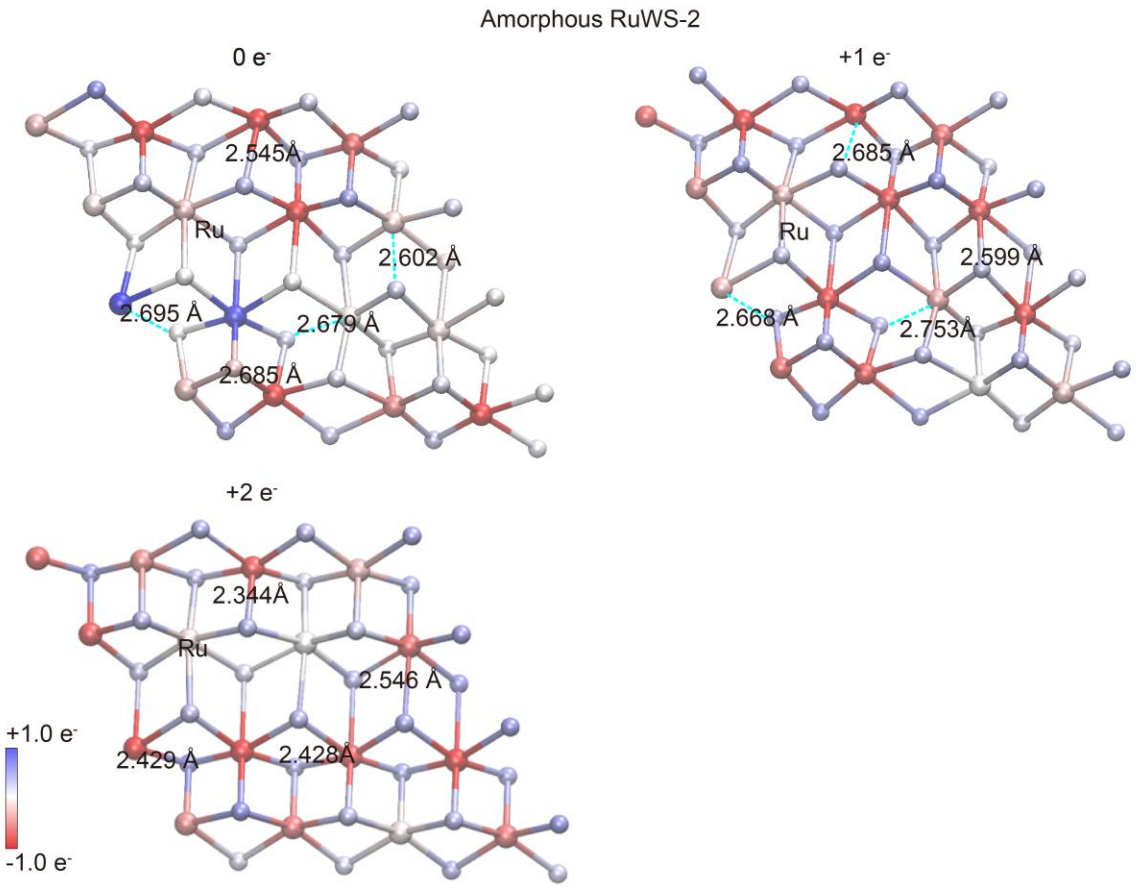

Fig. S63. Bader charge on amorphous RuWS-2 and relevant bond lengths before and after the electron injection.

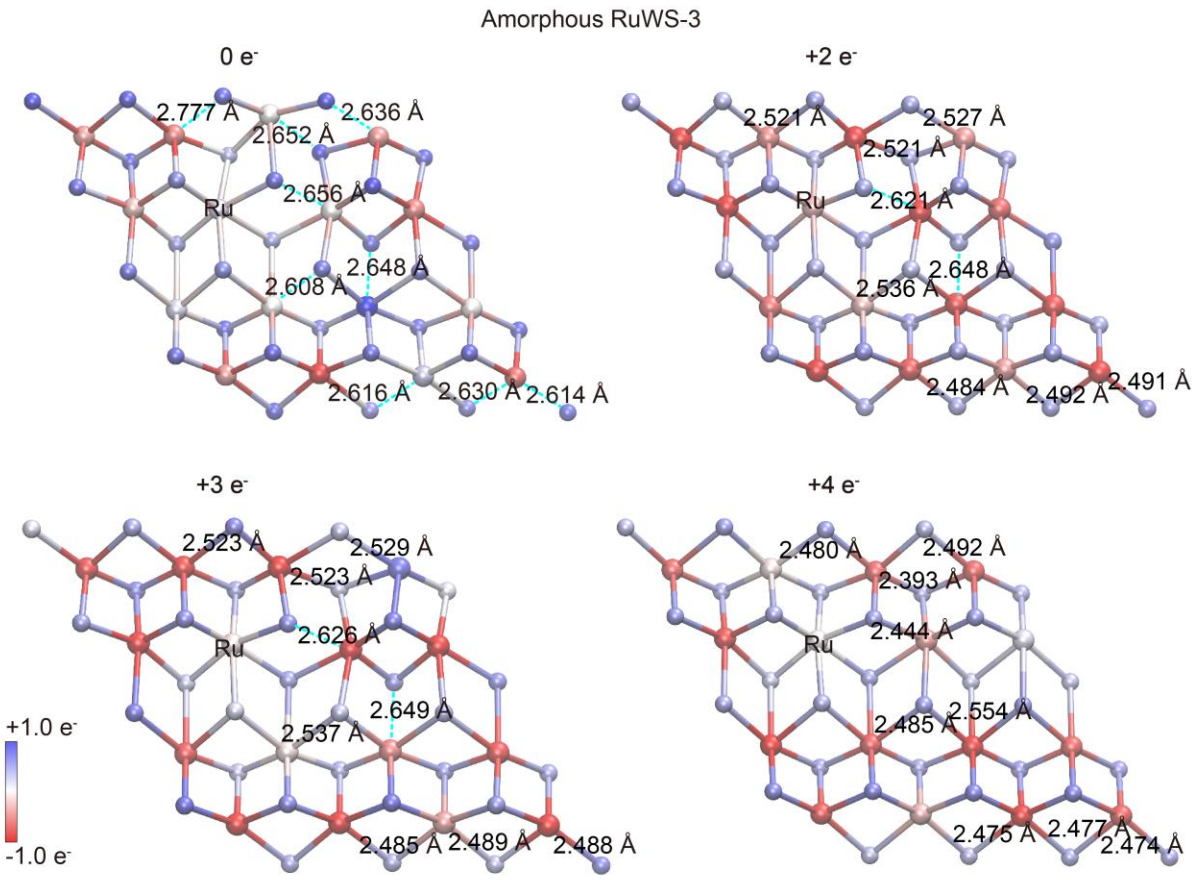

Fig. S64. Bader charge on amorphous RuWS-3 and relevant bond lengths before and after the electron injection.

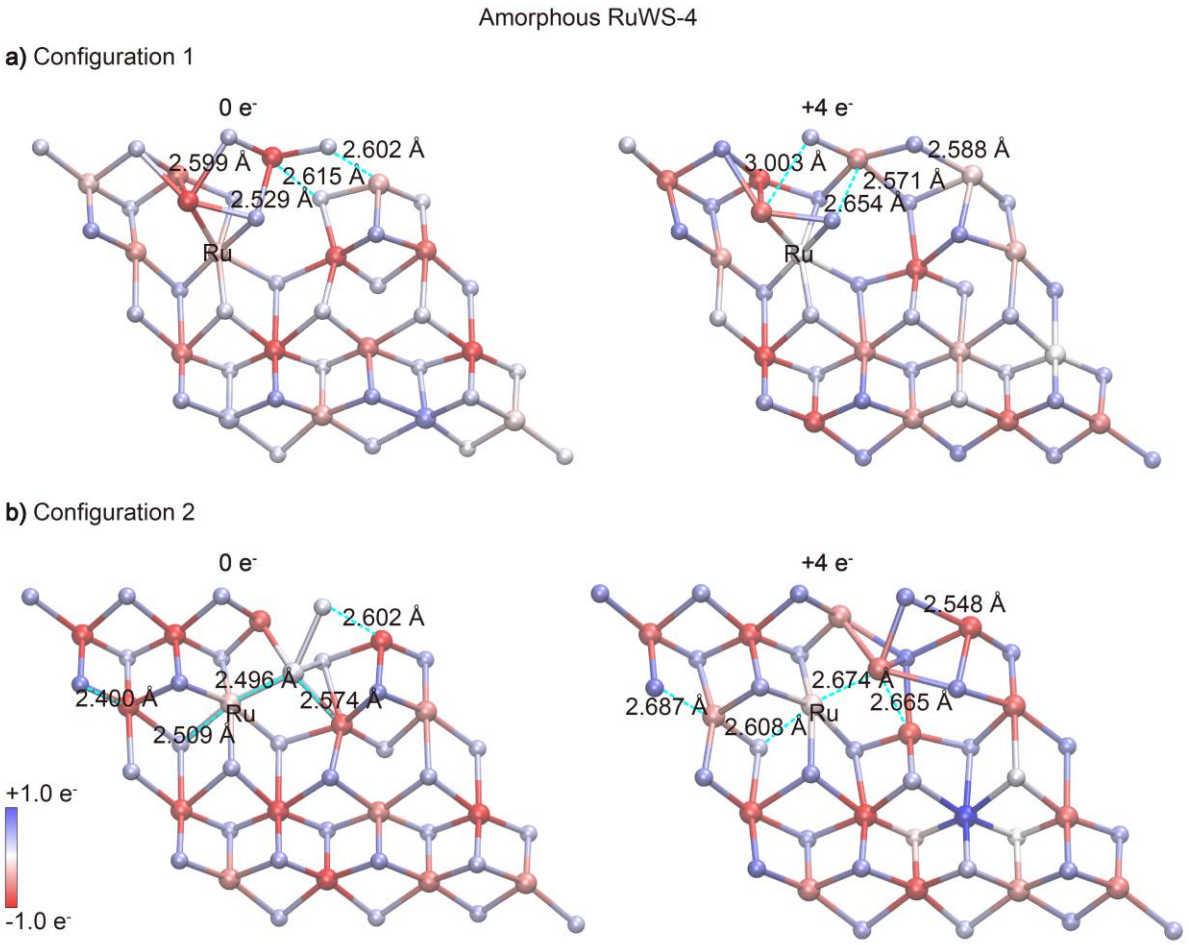

Fig. S65. Bader charge on amorphous RuWS-4 and relevant bond lengths before and after the electron injection.

3. Supplementary tables

Table S1. The Ru and W content of ICP results under 1000 mA cm^{-2} for 1600 h.

Element	Concentration in the electrolyte after test (μg/mL)	Relative decrease (%)
Ru	3.97	4.4
W	6.95	1.7

Table S2. Comparison of recently reported representative electrocatalysts for HER in 1.0 M KOH.

Catalysts	Overpotential at 10 mA cm^{-2} (mV)	Overpotential at 100 mA cm^{-2} (mV)	Overpotential at 1000 mA cm^{-2} (mV)	Tafel slope (mV dec^{-1})	Reference
a-RuWS	11.0	48.0	131	23.2	This work
Amorphous RuCo	24.9	88.1	~	40.5	[8]
c/a-Ru/VO_x-500	33.0	~		33.0	[9]
Pd_2RuO_x-0.5 h	14.0			25.6	[10]
Ru/Mo_2C/MoO_2	19.0	~50	160	18.3	[11]
MgO_x/MoO_y-Ru metallene	8.5			33.3	[12]
Cu-Ru/$RuSe_2$ NSs/C	23.0	109.0		58.5	[13]
Ru_c/NiFe-LDH	26.0	~50.0		67.4	[14]
Ru-a-CoNi	15.0	83.0		34.0	[15]
Ru/ac-$CeO_{2-\delta}$	21.2	~110.0		28.9	[16]
Ru-CrO_x@CN	7.0	~50.0		30.1	[17]
A-RuO_x	16.0	~80.0		30.3	[18]
RuS_x/S-GO	58.0	~137.0		34.0	[19]
Ru/ac-ZrO_2	14.0	~68.0	~170.0	26.9	[20]

Table S3. 1T-phase WS_2 content variation during electrochemical testing characterized by XPS.

Duration of the electrochemical test (h)	**Content (%)**
12	4.4
48	21.8
120	82.7

Table S4. Structural parameters of samples extracted from EXAFS fitting.

After test	Path	R (Å)	N_{coord}	σ^2 (Å2)	$\triangle E_0$ (eV)	R_f (%)
Initial	W-S	2.32±0.01	3.7±0.1	0.0025±0.0012	4.6±1.4	0.8
12 h	W-S	2.32±0.01	3.9±0.2	0.0031±0.0007	7.8±1.8	0.7
	W-W	2.58±0.03	3.3±0.4	0.0045±0.0017	6.5±0.9	
24 h	W-S	2.35±0.02	4.2±0.5	0.0035±0.0023	6.1±2.6	0.4
	W-W	2.63±0.04	3.5±0.1	0.0050±0.0028	4.0±1.5	
48 h	W-S	2.40±0.03	4.8±0.4	0.0057±0.0005	2.8±1.1	0.4
	W-W	2.71±0.13	4.0±0.3	0.0047±0.0062	3.1±1.0	
120 h	W-S	2.46±0.07	5.3±0.4	0.0028±0.0010	6.4±1.2	0.5
	W-W	2.75±0.03	4.2±0.4	0.0043±0.0021	2.3±0.9	

where R is the distance between absorber and backscatter atoms, N_{coord} is the coordination number, σ^2 is Debye–Waller factor, $\triangle E_0$ is the edge-energy shift, and R_f is the goodness of fit.

Table S5. Ru-S bond length of disordered structures before and after the electron injection.

Bond length/Å	1	2	3	4	5	6	average
Amorphous RuWS-1	2.39	2.444	2.435	2.447	2.405	2.394	2.419
Amorphous RuWS-1 +1 e^-	2.367	2.369	2.443	2.431	2.432	2.386	2.405
Amorphous RuWS-2	2.373	2.399	2.472	2.404	2.39	2.357	2.399
Amorphous RuWS-2 +1 e^-	2.374	2.491	2.531	2.435	2.397	2.417	2.441
Amorphous RuWS-2 +2 e^-	2.386	2.436	2.437	2.455	2.375	2.373	2.41
Amorphous RuWS-3	2.419	2.453	2.575	2.397	2.397	2.341	2.43
Amorphous RuWS-3 +2 e^-	2.381	2.413	2.441	2.443	2.401	2.393	2.412
Amorphous RuWS-3 +3 e^-	2.382	2.412	2.442	2.442	2.4	2.396	2.412
Amorphous RuWS-3 +4 e^-	2.383	2.442	2.439	2.46	2.381	2.377	2.414

4. References

1. Cui, Y.; Zhu, H.; Cai, J.; Qiu, H., Self-Regulated Co-Assembly of Soft and Hard Nanoparticles. *Nature Communications* **2021,** *12* (1), 5682.
2. Kresse, G., Furthmüller, J., Efficient Iterative Schemes for ab initio Total-Energy Calculations Using a Plane-Wave Basis Set. *Phy. Rev. B* **1996,** *54*, 11169-11186.
3. Kresse, G., Joubert, D., Projector Augmented-Wave Method, *Phy. Rev. B* **1999,** *59*, 1758-1775.
4. Blöchl, P. E., Projector Augmented-Wave Method. *Phy. Rev. B* **1994,** *50* (24), 17953-17979.
5. John P. Perdew, K. B., Matthias Ernzerhof, Generalized Gradient Approximation Made Simple. *Phys. Rev. Lett.* **1996,** *77*, 3865-3868.
6. Grimme, S.; Antony, J.; Ehrlich, S.; Krieg, H., A Consistent and Accurateab Initioparametrization of Density Functional Dispersion Correction (DFT-D) for the 94 Elements H-Pu. *J. Chem. Phys.* **2010,** *132* (15), 154104.
7. Wang, V.; Xu, N.; Liu, J.-C.; Tang, G.; Geng, W.-T., Vaspkit: A User-Friendly Interface Facilitating High-Throughput Computing and Analysis Using Vasp Code. *Comput. Phys. Commun.* **2021,** *267*, 108033.
8. Jose, V.; Do, V. H.; Prabhu, P.; Peng, C. K.; Chen, S. Y.; Zhou, Y.; Lin, Y. G.; Lee, J. M., Activating Amorphous Ru Metallenes through Co Integration for Enhanced Water Electrolysis. *Adv. Energy Mater.* **2023,** *13* (28), 2301119.
9. Tao, Z.; Zhao, H.; Lv, N.; Luo, X.; Yu, J.; Tan, X.; Mu, S., WS_2 Moiré Superlattices Supporting Au Nanoclusters and Isolated Ru to Boost Hydrogen Production. *Adv. Funct. Mater.* **2024,** *34* (19), 2312987.
10. Do, V. H.; Prabhu, P.; Jose, V.; Yoshida, T.; Zhou, Y.; Miwa, H.; Kaneko, T.; Uruga, T.; Iwasawa, Y.; Lee, J. M., Pd-PdO Nanodomains on Amorphous Ru Metallene Oxide for High-Performance Multifunctional Electrocatalysis. *Adv. Mater.* **2023,** *35* (12), 2208860.
11. Hou, L.; Li, C.; Jang, H.; Kim, M. G.; Jiang, J. Z.; Cho, J.; Liu, S.; Liu, X., Rationally Designed Mo/Ru-Based Multi-Site Heterogeneous Electrocatalyst for Accelerated Alkaline Hydrogen Evolution Reaction. *Adv. Mater.* **2024,** *36* (48), 2410039.
12. Tian, F.; Geng, S.; Li, M.; Qiu, L.; Wu, F.; He, L.; Sheng, J.; Zhou, X.; Chen, Z.; Luo, M.; Liu, H.; Yu, Y.; Yang, W.; Guo, S., Synergetic Oxidized Mg and Mo Sites on Amorphous Ru Metallene Boost Hydrogen Evolution Electrocatalysis. *Adv. Mater.* **2025,** *37*, 2501230.
13. Wang, K.; Zhou, J.; Sun, M.; Lin, F.; Huang, B.; Lv, F.; Zeng, L.; Zhang, Q.; Gu, L.; Luo, M.;

Guo, S., Cu-Doped Heterointerfaced Ru/$RuSe_2$ Nanosheets with Optimized H and H_2O Adsorption Boost Hydrogen Evolution Catalysis. *Adv. Mater.* **2023,** *35* (23), 2300980.

14. Zhu, Y.; Chen, Y.; Feng, Y.; Meng, X.; Xia, J.; Zhang, G., Constructing Ru-O-Tm Bridge in NiFe-LDH Enables High Current Hydrazine-Assisted H_2 Production. *Adv. Mater.* **2024,** *36* (30), 2401694.
15. Liu, Y.; Liu, X.; Jadhav, A. R.; Yang, T.; Hwang, Y.; Wang, H.; Wang, L.; Luo, Y.; Kumar, A.; Lee, J.; Bui, H. T. D.; Gyu Kim, M.; Lee, H., Unraveling the Function of Metal-Amorphous Support Interactions in Single-Atom Electrocatalytic Hydrogen Evolution. *Angew. Chem. Int. Ed.* **2022,** *61* (9), e202114160.
16. Qin, Q.; Jang, H.; Jiang, X.; Wang, L.; Wang, X.; Kim, M. G.; Liu, S.; Liu, X.; Cho, J., Constructing Interfacial Oxygen Vacancy and Ruthenium Lewis Acid-Base Pairs to Boost the Alkaline Hydrogen Evolution Reaction Kinetics. *Angew. Chem. Int. Ed.* **2023,** *63* (3), e202317622.
17. Zhang, B.; Wang, J.; Liu, G.; Weiss, C. M.; Liu, D.; Chen, Y.; Xia, L.; Zhou, P.; Gao, M.; Liu, Y.; Chen, J.; Yan, Y.; Shao, M.; Pan, H.; Sun, W., A Strongly Coupled Ru-CrO_x Cluster-Cluster Heterostructure for Efficient Alkaline Hydrogen Electrocatalysis. *Nat. Catal.* **2024,** *7* (4), 441-451.
18. Wu, B.; Liu, X.; Liu, P.; Wu, G.; Tian, L.; Han, X.; Li, J.; Hong, X., Synthesis of Amorphous Metal Oxides via a Crystalline to Amorphous Phase Transition Strategy. *Nat. Synth.* **2025,** *4* (3), 370-379
19. Li, P.; Duan, X.; Wang, S.; Zheng, L.; Li, Y.; Duan, H.; Kuang, Y.; Sun, X., Amorphous Ruthenium-Sulfide with Isolated Catalytic Sites for Pt-Like Electrocatalytic Hydrogen Production over Whole pH Range. *Small* **2019,** *15* (46), 1904043.
20. Niu, J.; Duan, H.; Sun, T.; Zhi, Z.; Li, D.; Fan, X.; Zhang, L.; Yang, D., Amorphous/Crystalline ZrO_2 with Oxygen Vacancies Anchored Nano-Ru Enhance Reverse Hydrogen Spillover in Alkaline Hydrogen Evolution. *Small* **2025**, 2410436.